Calculations of Polarization Observables in Pseudoscalar Meson Photo-production and Experimental Constraints on the $\gamma p \to K\Lambda$ Multipoles

A. M. Sandorfi,[1] S. Hoblit,[2,3] H. Kamano,[1] and T.-S. H. Lee[4,1]

[1]*Thomas Jefferson National Accelerator Facility, Newport News, Virginia 23606, USA*

[2]*Department of Physics, University of Virginia, Charlottesville, Virginia 22901, USA*

[3]*National Nuclear Data Center, Brookhaven National Laboratory, Upton, New York 11973, USA*

[4]*Physics Division, Argonne National Laboratory, Illinois 60439, USA*

(Dated: October 22, 2010)

Abstract

In preparation for a new generation of complete experiments with the goal of performing a high precision extraction of pseudoscalar meson photo-production amplitudes, we present expressions that allow the direct numerical calculation of matrix elements with arbitrary spin projections from Chew-Goldberger-Low-Nambu (CGLN) amplitudes. We use this numerical tool to verify the most general analytic form of the cross section, dependent upon the three polarization vectors of the beam, target and recoil baryon, including all single, double and triple-polarization terms involving 16 spin-dependent observables. Analytic expressions that determine the recoil baryon polarization are presented, together with examples of their potential use with quasi-4π detectors to deduce observables. We assemble the analytic equations relating the 16 experimental observables and the CGLN amplitudes and use our independent method of numerical evaluation to resolve sign differences that exist in the literature. Comparing to the MAID and SAID Partial Wave Analysis (PWA) codes, we have found that the implied definitions of six double-polarization observables are the negative of what has been used in comparing to recent experimental data, while the calculations of the BoGa PWA code are consistent with the present work. We have numerically checked the signs in the 37 Fierz identities that interrelate the 16 spin observables and have corrected many inconsistencies found in the literature. As an illustration of the use of this machinery, we carry out a multipole analysis of the $\gamma p \to K^+\Lambda$ reaction and examine the impact of recently published polarization measurements. When combining data from different experiments, we utilize the Fierz identities to fit a consistent set of scales. In fitting multipoles, we use a combined Monte Carlo sampling of the amplitude space, with gradient minimization, and find a shallow χ^2 valley pitted with a very large number of local minima. This results in broad bands of multipole solutions that are experimentally indistinguishable. While these bands are noticeably narrowed by the inclusion of additional polarization measurements, many of the multipoles remain very poorly determined, even in sign, despite the inclusion of recent data on 8 different observables. We have compared multipoles from recent PWA codes with our model-independent solution bands, and found that such comparisons provide useful consistency tests which clarify model interpretations, for example regarding the nature of the recently reported $N^*(\sim 1900)$. We conclude that, while a mathematical solution to the problem of determining an amplitude free of ambiguities may require 8 observables, as has been pointed out in the literature, experiments with realistically achievable uncertainties will require a significantly larger number.

PACS numbers: 13.60.Le, 13.75.Gx, 13.75.Jz

I. INTRODUCTION

As a consequence of dynamic chiral symmetry breaking, the Goldstone bosons (π, η, K) dress the nucleon and alter its spectrum. Not surprisingly, pseudoscalar meson production has been a powerful tool in studying the spectrum of excited nucleon states. However, such states are short lived and broad so that above the energy of the first resonance, the P_{33} $\Delta(1232)$, the excitation spectrum is a complicated overlap of many resonances. Isolating any one and separating it from backgrounds has been a long-standing problem in the literature.

The spin degrees of freedom in meson photoproduction provide signatures of interfering partial wave strength that are often dramatic and have been useful for differentiating between models of meson production amplitudes. Models that must account for interfering resonance amplitudes and non-resonant contributions are often severely challenged by new polarization data. Ideally, one would like to partition the problem by first determining the amplitudes from experiment, at least to within a phase, and then relying upon a model to separate resonances from non-resonant processes. Single-pseudoscalar photoproduction is described by 4 complex amplitudes (two for the spin states of the photon, two for the nucleon target and two for the baryon recoil, which parity considerations reduces to a total of 4). To avoid ambiguities, it was shown [1] that angular distribution measurements of at least 8 carefully chosen observables at each energy for both proton and neutron targets must be performed. While such experimental information has not yet been available, even after 50 years of photoproduction experiments, a sequence of *complete* experiments are now underway at Jefferson Lab [2, 3], as well as complementary experiments from the GRAAL backscattering source in Grenoble [4, 5] and the electron facilities in Bonn and Mainz, with the goal of obtaining a direct determination of the amplitude to within a phase, for at least a few production channels, notably $K\Lambda$ and possibly πN.

Our purpose here is two fold. First we assemble the relations between experimental observables and the Chew-Goldberger-Low-Nambu (CGLN) amplitudes and electromagnetic multipoles [6], and resolve sign differences that exist in the literature. Then, as an illustration of the use of these relations along the path to determining an amplitude from the new generation of experiments, we use recently published results on 8 different observables to carry out a multipole analysis of the $\gamma p \to K^+\Lambda$ reaction, free of model assumptions, and evaluate the uniqueness of the resulting solutions.

The four CGLN amplitudes can be expressed in Cartesian (F_i), Spherical or Helicity (H_i), or Transversity (b_i) representations. While the latter two choices afford some theoretical simplifications when predicting asymmetries from model amplitudes [7], when working in the reverse direction, fitting asymmetries to extract amplitudes, such simplifications are largely moot. In practice, one expands the amplitudes in multipoles and fits the multipoles directly. This both facilitates the search for resonance behavior and allows the use of full angular distribution data at a fixed energy to constrain angle-independent quantities. (Extracting the four CGLN amplitudes directly would require separate fits at each angle, along with some way of constraining an arbitrary phase which could be angle dependent.) Here we restrict our considerations to the CGLN F_i representation, which has the simplest decomposition into multipoles [6], Eqs. (15)-(18) below.

In single-pseudoscalar meson photoproduction there are 16 possible observables, the unpolarized differential cross section ($d\sigma_0$), three asymmetries which to leading order enter the general cross section scaled by a single polarization of either beam, target or recoil (Σ, T, P), and three sets of four asymmetries whose leading dependence in the general cross section involves two polarizations of either beam-target (BT), beam-recoil (BR), or target-recoil (TR), as in Ref. [7]. Expressions for at least some of these observables in terms of the CGLN F_i appear already in earlier papers [8, 9]. The available complete expressions can be classified into two groups of Refs. [10, 11] and Refs. [12, 13]. In all cases we have found in the literature, the magnitudes of the expressions relating the CGLN F_i to experimental observables are identical, but the signs of some appear to differ. In particular, sign differences have occurred in double-polarization observables for which little data have been available until very recently. There is also a set of 37 *Fierz* identities interrelating the 16 polarization observables, the most complete list being given in Ref. [1]. We have found many of the signs in the expressions of this list to be incompatible with either group of papers, Ref. [10, 11] or [12, 13].

There are several coordinate systems in use in the literature and in Sec. II we define ours, which is the same as used in the seminal paper by Barker, Donnachie and Storrow (BDS) [7]. In Sec. III we present explicit and complete formulae that allow the direct calculation of matrix elements with arbitrary spin projections from CGLN amplitudes or multipoles. In Sec. IV we present the most general analytic form of the cross section, dependent on the three

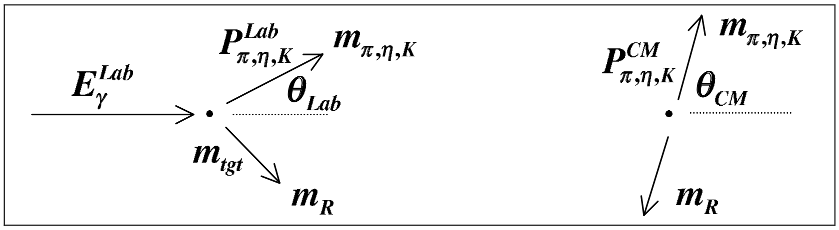

FIG. 1: Kinematic variables in meson photoproduction in Lab and CM frames.

polarization vectors of the beam, the target and the recoil baryon. The derivation of this cross section expression is summarized in Appendix A, and the experimental definitions of the observables in terms of cross sections with explicit polarization orientations is tabulated in Appendix B. Using these definitions, numerical evaluations of the expressions in Sec. III are used to verify the consistency of the signs in the analytic general cross section equation of Sec. IV. While the beam and target polarizations are under experimental control, the recoil polarization is on a very different footing, being a byproduct of the angular momentum of the entrance channel and the reaction physics. Expressions that determine the recoil baryon polarization are developed in Sec. V. To evaluate the analytic relations between observables and amplitudes we next use numerical calculations of the expressions in Sec. III to fix signs and present the complete set of equations in Sec. VI that determine the 16 observables from the CGLN amplitudes. The 37 Fierz identities that interrelate the observables are discussed in Sec. VII and presented with corrected signs in Appendix C. In Sec. VIII we utilize the machinery we have assembled to carry out a multipole analysis of the $\gamma p \to K^+\Lambda$ reaction. (Born terms for this process are summarized in Appendix D.) In so doing we test the nature of the χ^2 valley, discuss the role of the arbitrary phase and examine the impact of recently published polarization data and the uniqueness of the multipole solution. Section IX concludes with a brief summary.

II. KINEMATICS AND COORDINATE DEFINITIONS

The kinematic variables of meson photoproduction used in our derivations are specified in Fig. 1. Some useful relations are :

- The total center of mass (CM) energy:

$$W = \sqrt{s} = \sqrt{m_{\rm tgt}(m_{\rm tgt} + 2E_\gamma^{\rm Lab})}. \tag{1}$$

- The laboratory (Lab) energy needed to excite the hadronic system with total CM energy W:

$$E_\gamma^{\text{Lab}} = \frac{W^2 - m_{\text{tgt}}^2}{2m_{\text{tgt}}}. \tag{2}$$

- The energy of the photon in the CM frame:

$$E_\gamma^{\text{CM}} = \frac{W^2 - m_{\text{tgt}}^2}{2W} = q. \tag{3}$$

- The magnitude of the 3-momentum of the meson in the CM frame:

$$\left|P_{\pi,\eta,K}^{\text{CM}}\right| = \frac{W}{2}\left\{\left[1-\left(\frac{m_{\pi,\eta,K}+m_R}{W}\right)^2\right]\left[1-\left(\frac{m_{\pi,\eta,K}-m_R}{W}\right)^2\right]\right\}^{1/2} = k. \tag{4}$$

- The density of state factor:

$$\rho_0 = \left|P_{\pi,\eta,K}^{\text{CM}}\right| / E_\gamma^{\text{CM}} = k/q. \tag{5}$$

The definitions of polarization angles used in our derivation are shown in Fig. 2, using the case of K Λ production as an example. The $\langle \hat{x} - \hat{z} \rangle$ plane is the reaction plane in the center of mass. The figure illustrates the case of linear γ polarization, with the alignment direction P_L^γ (parallel to the oscillating electric field of the photon) in the $\langle \hat{x} - \hat{y} \rangle$ plane at an angle ϕ_γ, rotating from $\hat{x}$ towards $\hat{y}$. The target nucleon polarization $\vec{P}^T$ is specified by polar angle θ_p measured from $\hat{z}$, and azimuthal angle ϕ_p in the $\langle \hat{x} - \hat{y} \rangle$ plane, rotating from $\hat{x}$ towards $\hat{y}$. The recoil Λ baryon is in the $\langle \hat{x} - \hat{z} \rangle$ plane; its polarization $\vec{P}_\Lambda^R$ is at polar $\theta_{p'}$, measured from $\hat{z}$, and azimuthal $\phi_{p'}$ in the $\langle \hat{x} - \hat{y} \rangle$ plane, rotating from $\hat{x}$ to $\hat{y}$. Following BDS [7], observables involving recoil polarization are specified in the rotated coordinate system with $\hat{z}' = +\hat{k}$, along the meson CM momentum and opposite the recoil momentum, $\hat{y}' = \hat{y}$, and $\hat{x}' = \hat{y}' \times \hat{z}'$ in the scattering plane at a polar angle of $\theta_K + (\pi/2)$ relative to $\hat{z}$.

The case of circular photon polarization can potentially lead to some confusion. Most particle physics literature designates circular states as r, for right circular (or l, for left circular), referring to the fact that with r polarization the electric vector of the photon appears to rotate clockwise *when the photon is traveling away from the observer*. However, when the same photon is viewed by an observer facing the incoming photon the electric vector appears to rotate counter-clockwise. For this reason optics literature traditionally designates this same state as l circularly polarized. Nonetheless, both conventions agree on

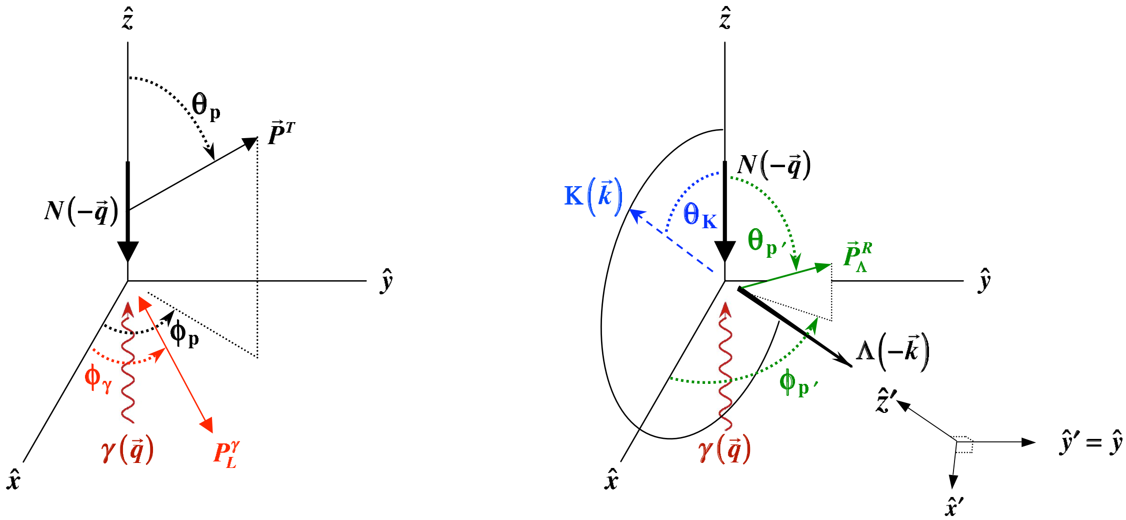

FIG. 2: The CM coordinate system and angles used to specify polarizations in the reaction, $\gamma(\vec{q}, \vec{P}^\gamma) + N(-\vec{q}, \vec{P}^T) \to K(\vec{k}) + \Lambda(-\vec{k}, \vec{P}^R_\Lambda)$. The left (right) side is for the initial γN (final $K\Lambda$ system.

the value of the photon helicity [14] $h = \vec{S} \cdot \vec{P}/|\vec{P}| = \pm 1$ and so we use only the helicity designations here, $\vec{P}^\gamma_c = +1(-1)$ when 100% of the photon spins are parallel (anti-parallel) to the photon momentum vector.

III. CALCULATION OF POLARIZATION OBSERVABLES

As discussed in Sec. I, all publications give similar formulae for polarization observables, but conflicting signs occur in some terms with very lengthy expressions. It is very difficult, if not impossible, to resolve this problem by repeating the same algebraic procedures used in previous works. To resolve these sign problems, it is necessary to develop completely different and yet simple formulae which can be used to calculate numerically all spin observables of pseudoscalar meson photoproduction. This numerical tool will then allow us to check unambiguously the analytic expressions for spin observables in all previous publications. In this section, we present the derivation of such formulae using the case of $K\Lambda$ photoproduction as an example.

Let us first consider the case when all beam, target, and recoil polarizations are 100% polarized in certain directions. With variables specified as in Fig. 2, the differential cross section for $\gamma(\vec{q}, \hat{P}^\gamma) + N(-\vec{q}, m_{s_N}) \to K(\vec{k}) + \Lambda(-\vec{k}, m_{s_\Lambda})$ in the center of mass frame can be written as

$$\frac{d\sigma}{d\Omega}(\hat{P}^\gamma, m_{s_N}, m_{s_\Lambda}) = \frac{1}{(4\pi)^2}\frac{k}{q}\frac{m_N m_\Lambda}{W^2}|\bar{u}_\Lambda(-\vec{k}, m_{s_\Lambda})I^\mu \epsilon_\mu u_N(-\vec{q}, m_{s_N})|^2, \tag{6}$$

where $W = q + E_N(q) = E_K(k) + E_\Lambda(k)$; $\epsilon_\mu = (0, \hat{P}^\gamma)$ with $|\hat{P}^\gamma| = 1$ is the photon polarization vector; m_{s_Λ} and m_{s_N} are the spin substate quantum numbers of the Λ and the nucleon along the z-direction, respectively; $\bar{u}_\Lambda I^\mu \epsilon_\mu u_N$ is normalized to the usual invariant amplitude calculated from a Lagrangian in the convention of Bjorken and Drell [15]. For example, for a simplified Lagrangian density $L(x) = -(f_{K\Lambda N}/m_K)\bar{\psi}_\Lambda(x)\gamma_5\gamma_\mu\psi_N(x)\partial^\mu\phi_K(x) + e_N\bar{\psi}_N(x)\gamma^\mu\psi_N(x)A_\mu(x)$, the s-channel $\gamma(q) + N(p) \rightarrow N(p' + k) \rightarrow K^+(k) + \Lambda(p')$ contribution to I^μ is $ie_N(f_{K\Lambda N}/m_K)\ \not{k}\gamma_5[(\not{k}+\ \not{p}') - m_N]^{-1}\gamma^\mu$. By averaging over all initial state polarizations and summing over final state polarizations in Eq. (6), we can obtain the unpolarized cross section:

$$d\sigma_0 \equiv \frac{1}{4}\sum_{m_{s_N}=\pm 1/2}\sum_{m_{s_\Lambda}=\pm 1/2}\sum_{\gamma\text{-spins}}\frac{d\sigma}{d\Omega}(\hat{P}^\gamma, m_{s_N}, m_{s_\Lambda}), \tag{7}$$

where the symbol $\sum_{\gamma\text{-spins}}$ implies taking summation over two photon polarization states, with polarization vectors perpendicular to each other for linearly polarized photons and with helicity ± 1 states for circularly polarized photons.

The CGLN amplitude [6] is defined by

$$\bar{u}_\Lambda(-\vec{k}, m_{s_\Lambda})I^\mu \epsilon_\mu u_N(-\vec{q}, m_{s_N}) = -\frac{4\pi W}{\sqrt{m_N m_\Lambda}}\langle m_{s_\Lambda}|F_{\rm CGLN}|m_{s_N}\rangle, \tag{8}$$

where $|m_s\rangle$ is the usual eigenstate of the Pauli operator σ_z, and

$$F_{\rm CGLN} = \sum_{i=1,4} O_i F_i(\theta_K, E), \tag{9}$$

with

$$O_1 = -i\vec{\sigma}\cdot\hat{P}^\gamma, \tag{10}$$

$$O_2 = -[\vec{\sigma}\cdot\hat{k}][\vec{\sigma}\cdot(\hat{q}\times\hat{P}^\gamma)], \tag{11}$$

$$O_3 = -i[\vec{\sigma}\cdot\hat{q}][\hat{k}\cdot\hat{P}^\gamma], \tag{12}$$

$$O_4 = -i[\vec{\sigma}\cdot\hat{k}][\hat{k}\cdot\hat{P}^\gamma]. \tag{13}$$

Here we have defined $\hat{k} = \vec{k}/|\vec{k}|$ and $\hat{q} = \vec{q}/|\vec{q}|$. We then obtain

$$\frac{d\sigma}{d\Omega}(\hat{P}^\gamma, m_{s_N}, m_{s_\Lambda}) = \frac{k}{q}|\langle m_{s_\Lambda}|F_{\rm CGLN}|m_{s_N}\rangle|^2. \tag{14}$$

The formulae for calculating CGLN amplitudes from multipoles are well known [6] and are given below:

$$F_1 = \sum_{l=0}[P'_{l+1}(x)E_{l+} + P'_{l-1}(x)E_{l-} + lP'_{l+1}(x)M_{l+} + (l+1)P'_{l-1}(x)M_{l-}]\,, \tag{15}$$

$$F_2 = \sum_{l=0}[(l+1)P'_l(x)M_{l+} + lP'_l(x)M_{l-}]\,, \tag{16}$$

$$F_3 = \sum_{l=0}[P''_{l+1}(x)E_{l+} + P''_{l-1}(x)E_{l-} - P''_{l+1}(x)M_{l+} + P''_{l-1}(x)M_{l-}]\,, \tag{17}$$

$$F_4 = \sum_{l=0}[-P''_l(x)E_{l+} - P''_l(x)E_{l-} + P''_l(x)M_{l+} - P''_l(x)M_{l-}]\,. \tag{18}$$

where $x = \hat{k}\cdot\hat{q} = \cos\theta_K$, l is the orbital angular momentum of the $K\Lambda$ system, and $P'_l(x) = dP_l(x)/dx$ and $P''_l(x) = d^2P_l(x)/dx^2$ are the derivatives of the Legendre function $P_l(x)$, with the understanding that $P'_{-1} = P''_{-1} = 0$. In practice, the sum runs to a limiting value of l_{max} which depends on the energy.

In order to calculate the 16 polarization observables in an arbitrary experimental geometry, we develop a form for the cross section with arbitrary spin projections for initial and final baryon states, $\gamma(\vec{q},\hat{P}^\gamma) + N(-\vec{q},\hat{P}^T) \to K(\vec{k}) + \Lambda(-\vec{k},\hat{P}^R)$, as specified in Fig. 2, where $\hat{P}^T$ ($\hat{P}^R$) is the unit vector specifying the direction of the target (recoil) spin polarization. Here linear photon polarization must be in the $\langle\hat{x}-\hat{y}\rangle$ plane and circular photon polarization must be aligned with $\hat{z}$, while $\hat{P}^T$ and $\hat{P}^R$ can be in any directions. The corresponding cross section is obtained by simply replacing $|\langle m_{s_\Lambda}|F_{\mathrm{CGLN}}|m_{s_N}\rangle|^2$ in Eq. (14) with $|\langle\hat{P}^R|F_{\mathrm{CGLN}}|\hat{P}^T\rangle|^2$:

$$d\sigma_{\mathrm{B,T,R}}(\hat{P}^\gamma,\hat{P}^T,\hat{P}^R) \equiv \frac{d\sigma}{d\Omega}(\hat{P}^\gamma,\hat{P}^T,\hat{P}^R) = \frac{k}{q}|\langle\hat{P}^R|F_{\mathrm{CGLN}}|\hat{P}^T\rangle|^2, \tag{19}$$

where $|\hat{P}^T\rangle$ ($\langle\hat{P}^R|$) is a state of the initial (final) spin-1/2 baryon with the spin pointing in the $\hat{P}^T$ ($\hat{P}^R$) direction. We note that if $\hat{P}^T$ ($\hat{P}^R$) is in the direction of the momentum of the initial (final) baryon, then $|\hat{P}^T\rangle$ ($\langle\hat{P}^R|$) is the usual helicity state as defined, for example, by Jacob and Wick [16]. We need to consider more general spin orientations for all possible experiments geometries. The spin state $|\hat{s}\rangle$ quantized in the direction of an arbitrary vector $\hat{s} = (1,\theta,\phi)$ is defined by

$$\vec{S}\cdot\hat{s}|\hat{s}\rangle = +\frac{1}{2}|\hat{s}\rangle, \tag{20}$$

where $\vec{S}$ is the spin operator. For the considered spin-1/2 baryons, $\vec{S}$ is expressed with the Pauli matrix: $\vec{S} = \vec{\sigma}/2$.

We next derive explicit formulae for calculating the matrix element $\langle \hat{P}^R | F_{\rm CGLN} | \hat{P}^T \rangle$ in terms of the CGLN amplitudes F_i in Eqs. (15)-(18). We note that the spin state $|\hat{s}\rangle$ is related to the usual eigenstate of z-axis quantization by rotations:

$$|\hat{s}\rangle = \sum_{m=\pm 1/2} D^{(1/2)}_{m,+1/2}(\phi,\theta,-\phi)|m\rangle, \tag{21}$$

where $|m\rangle$ is defined as $S_z|\pm 1/2\rangle = (\pm 1/2)|\pm 1/2\rangle$, and

$$D^{(1/2)}_{m,\lambda}(\phi,\theta,-\phi) = e^{-i(m-\lambda)\phi} d^{1/2}_{m,\lambda}(\theta). \tag{22}$$

We use the phase convention of Brink and Satchler [17] where,

$$\begin{aligned} d^{1/2}_{+1/2,+1/2}(\theta) = d^{1/2}_{-1/2,-1/2}(\theta) = \cos\frac{\theta}{2}, \\ d^{1/2}_{-1/2,+1/2}(\theta) = -d^{1/2}_{+1/2,-1/2}(\theta) = \sin\frac{\theta}{2}. \end{aligned} \tag{23}$$

Equation (21) can be easily verified by explicit calculations using the definition (20) and the properties (22) and (23) for the special cases where $\hat{s} = \hat{x}$, $\hat{y}$, $\hat{z}$, together with the usual definition of the Pauli matrices, $(\sigma_i)_{mm'}$ [$i = x, y, z$ and m (row), m' (column) $= \pm 1/2, \pm 1/2$],

$$\sigma_x = \begin{pmatrix} 0 & 1 \\ 1 & 0 \end{pmatrix}, \ \sigma_y = \begin{pmatrix} 0 & -i \\ i & 0 \end{pmatrix}, \ \sigma_z = \begin{pmatrix} 1 & 0 \\ 0 & -1 \end{pmatrix}. \tag{24}$$

From Fig. 2, the momenta and linear photon polarization are expressed as

$$\vec{q} = q(0,0,1), \tag{25}$$

$$\vec{k} = k(\sin\theta_K, 0, \cos\theta_K), \tag{26}$$

$$\hat{P}^\gamma_L = (\cos\phi_\gamma, \sin\phi_\gamma, 0). \tag{27}$$

Circular photon polarizations of helicity λ_γ are expressed as

$$(\hat{P}^\gamma_c)_{\lambda_\gamma=\pm 1} = \mp\frac{1}{\sqrt{2}}(\hat{x} \pm i\hat{y}). \tag{28}$$

For the initial and final baryon polarizations, we use the spherical variables, as in Fig. 2:

$$\hat{P}^T = (1, \theta_p, \phi_p), \tag{29}$$

$$\hat{P}^R = (1, \theta_{p'}, \phi_{p'}). \tag{30}$$

TABLE I: $C_{i,n}(\theta_K, \phi_\gamma)$ of Eqs. (31) and (33)

	$n=0$	$n=1$	$n=2$	$n=3$
$i=1$	0	$-i\cos\phi_\gamma$	$-i\sin\phi_\gamma$	0
$i=2$	$\sin\theta_K\sin\phi_\gamma$	$i\cos\theta_K\cos\phi_\gamma$	$i\cos\theta_K\sin\phi_\gamma$	$-i\sin\theta_K\cos\phi_\gamma$
$i=3$	0	0	0	$-i\sin\theta_K\cos\phi_\gamma$
$i=4$	0	$-i\sin^2\theta_K\cos\phi_\gamma$	0	$-i\sin\theta_K\cos\theta_K\cos\phi_\gamma$

By using Eqs. (25)-(27), we can rewrite O_i in Eqs. (10)-(13) as

$$O_i = \sum_{n=0,3} C_{i,n}(\theta_K, \phi_\gamma)\sigma_n, \tag{31}$$

where $\sigma_0 = \mathbf{1}$, $\sigma_1 = \sigma_x$, $\sigma_2 = \sigma_y$, $\sigma_3 = \sigma_z$. The explicit form of $C_{i,n}$ is given in Table I.

By using Eq. (21) and Eqs. (9) and (31), the photoproduction matrix element can then be calculated as

$$\langle \hat{P}^R | F_{\rm CGLN} | \hat{P}^T \rangle = \sum_{n=0,3} G_n(\theta_K, \phi_\gamma) \langle \hat{P}^R | \sigma_n | \hat{P}^T \rangle, \tag{32}$$

with

$$G_n(\theta_K, \phi_\gamma) = \sum_{i=1,4} F_i(\theta_K, E) C_{i,n}(\theta_K, \phi_\gamma), \tag{33}$$

and

$$\langle \hat{P}^R | \sigma_n | \hat{P}^T \rangle = \sum_{m_{s_\Lambda}, m_{s_N} = \pm 1/2} D^{(1/2)*}_{m_{s_\Lambda}, +1/2}(\phi_{p'}, \theta_{p'}, -\phi_{p'}) D^{(1/2)}_{m_{s_N}, +1/2}(\phi_p, \theta_p, -\phi_p) \langle m_{s_\Lambda} | \sigma_n | m_{s_N} \rangle, \tag{34}$$

where $\langle m_{s_\Lambda} | \sigma_n | m_{s_N} \rangle = (\sigma_n)_{m_{s_\Lambda}, m_{s_N}}$ are the elements of the Pauli matrices of Eq. (24).

We may now start with any set of multipoles and use Eqs. (15)-(18) to calculate the CGLN amplitudes, which are then used to calculate the matrix element $\langle \hat{P}^R | F_{\rm CGLN} | \hat{P}^T \rangle$ by using Eqs. (32)-(34). Equation (19) then allows us to calculate all possible polarization observables, for the case of unit polarization vectors with arbitrary orientation.

With non-unit polarization vectors, the general cross section can be expressed in terms of Eq. (19) as, (see also Appendix A),

$$d\sigma_{\rm B,T,R}(\vec{P}^\gamma, \vec{P}^T, \vec{P}^R) = \sum_{\hat{P} = \hat{P}_1^\gamma, \hat{P}_2^\gamma} \sum_{\hat{Q} = \pm \hat{P}^T} \sum_{\hat{R} = \pm \hat{P}^R} \mathfrak{p}^\gamma_{\hat{P}} \mathfrak{p}^T_{\hat{Q}} \mathfrak{p}^R_{\hat{R}} \, d\sigma_{\rm B,T,R}(\hat{P}, \hat{Q}, \hat{R}). \tag{35}$$

Here the vector $\vec{P}^X$ specifies the degree and direction of the polarization of particle $X = \gamma, T, R$. For the target (T) and recoil (R) baryons, this is just $\vec{P}^X = (\mathfrak{p}^X_{+\hat{P}^X} - \mathfrak{p}^X_{-\hat{P}^X})\hat{P}^X$, where $\mathfrak{p}^X_{\pm\hat{P}^X}$ $(X = T, R)$ is the probability of observing X with its polarization vector pointing in the $\pm\hat{P}^X$ direction. For the photons (γ), however, the non-unit polarization vector can be expressed as $\vec{P}^\gamma = (\mathfrak{p}^\gamma_{\hat{P}^\gamma_1} - \mathfrak{p}^\gamma_{\hat{P}^\gamma_2})\hat{P}^\gamma$. Here, $\hat{P}^\gamma_1$ ($\equiv \hat{P}^\gamma$) and $\hat{P}^\gamma_2$ are orthogonal polarization directions, 90° apart for linear polarization, and opposite helicity states for circular polarization. Then $\mathfrak{p}^\gamma_{\hat{P}^\gamma_1}$ ($\mathfrak{p}^\gamma_{\hat{P}^\gamma_2}$) is a probability observing photons with its polarization vector pointing in the $\hat{P}^\gamma_1$ ($\hat{P}^\gamma_2$) direction. To clarify Eq. (35), consider the case that all beam, target, and recoil particles are unpolarized as an example. In this case the probabilities of finding spin projection in each of two possible directions are equal and hence $\mathfrak{p}^{T,R}_{\pm\hat{P}^{T,R}} = \mathfrak{p}^\gamma_{\hat{P}^\gamma_1,\hat{P}^\gamma_2} = 1/2$, which lead to $\vec{P}^{\gamma,T,R} = \vec{0}$. Then we have

$$\begin{aligned}
d\sigma_{\mathrm{B,T,R}}(\vec{0},\vec{0},\vec{0}) &= \frac{1}{8}\Big[d\sigma_{\mathrm{B,T,R}}(\hat{P}^\gamma_1, +\hat{P}^T, +\hat{P}^R) + d\sigma_{\mathrm{B,T,R}}(\hat{P}^\gamma_1, +\hat{P}^T, -\hat{P}^R) \\
&\quad + d\sigma_{\mathrm{B,T,R}}(\hat{P}^\gamma_1, -\hat{P}^T, +\hat{P}^R) + d\sigma_{\mathrm{B,T,R}}(\hat{P}^\gamma_1, -\hat{P}^T, -\hat{P}^R) \\
&\quad + d\sigma_{\mathrm{B,T,R}}(\hat{P}^\gamma_2, +\hat{P}^T, +\hat{P}^R) + d\sigma_{\mathrm{B,T,R}}(\hat{P}^\gamma_2, +\hat{P}^T, -\hat{P}^R) \\
&\quad + d\sigma_{\mathrm{B,T,R}}(\hat{P}^\gamma_2, -\hat{P}^T, +\hat{P}^R) + d\sigma_{\mathrm{B,T,R}}(\hat{P}^\gamma_2, -\hat{P}^T, -\hat{P}^R)\Big] \\
&= \frac{1}{2}d\sigma_0,
\end{aligned} \tag{36}$$

where $d\sigma_0$ is the unpolarized cross section defined in Eq. (7). The appearance of the factor (1/2) in the last equation is because the polarization of the final recoil particles is also averaged in Eq. (36).

IV. GENERAL CROSS SECTION

The derivation of an analytic expression for the general cross section in pseudoscalar meson photoproduction is summarized in Appendix A, where we follow the formalism of Fasano, Tabakin and Saghai (FTS) [11], expanding their treatment to include the complete set of triple polarization cases. In terms of the polarization vectors of Fig. 2, and with sign verified numerically using Eq. (35) of Sec. III, the most general form of the cross section can be written as,

$$
\begin{aligned}
d\sigma_{\mathrm{B,T,R}}(\vec{P}^{\gamma}, \vec{P}^{T}, \vec{P}^{R}) \;=\; \frac{1}{2}\Big\{ & d\sigma_0 \left[1 - P_L^{\gamma} P_y^T P_{y'}^R \cos(2\phi_\gamma)\right] \\
& + \hat{\Sigma} \left[-P_L^{\gamma} \cos(2\phi_\gamma) + P_y^T P_{y'}^R\right] \\
& + \hat{T} \left[P_y^T - P_L^{\gamma} P_{y'}^R \cos(2\phi_\gamma)\right] \\
& + \hat{P} \left[P_{y'}^R - P_L^{\gamma} P_y^T \cos(2\phi_\gamma)\right] \\
& + \hat{E} \left[-P_c^{\gamma} P_z^T + P_L^{\gamma} P_x^T P_{y'}^R \sin(2\phi_\gamma)\right] \\
& + \hat{G} \left[P_L^{\gamma} P_z^T \sin(2\phi_\gamma) + P_c^{\gamma} P_x^T P_{y'}^R\right] \\
& + \hat{F} \left[P_c^{\gamma} P_x^T + P_L^{\gamma} P_z^T P_{y'}^R \sin(2\phi_\gamma)\right] \\
& + \hat{H} \left[P_L^{\gamma} P_x^T \sin(2\phi_\gamma) - P_c^{\gamma} P_z^T P_{y'}^R\right] \\
& + \hat{C}_{x'} \left[P_c^{\gamma} P_{x'}^R - P_L^{\gamma} P_y^T P_{z'}^R \sin(2\phi_\gamma)\right] \\
& + \hat{C}_{z'} \left[P_c^{\gamma} P_{z'}^R + P_L^{\gamma} P_y^T P_{x'}^R \sin(2\phi_\gamma)\right] \\
& + \hat{O}_{x'} \left[P_L^{\gamma} P_{x'}^R \sin(2\phi_\gamma) + P_c^{\gamma} P_y^T P_{z'}^R\right] \\
& + \hat{O}_{z'} \left[P_L^{\gamma} P_{z'}^R \sin(2\phi_\gamma) - P_c^{\gamma} P_y^T P_{x'}^R\right] \\
& + \hat{L}_{x'} \left[P_z^T P_{x'}^R + P_L^{\gamma} P_x^T P_{z'}^R \cos(2\phi_\gamma)\right] \\
& + \hat{L}_{z'} \left[P_z^T P_{z'}^R - P_L^{\gamma} P_x^T P_{x'}^R \cos(2\phi_\gamma)\right] \\
& + \hat{T}_{x'} \left[P_x^T P_{x'}^R - P_L^{\gamma} P_z^T P_{z'}^R \cos(2\phi_\gamma)\right] \\
& + \hat{T}_{z'} \left[P_x^T P_{z'}^R + P_L^{\gamma} P_z^T P_{x'}^R \cos(2\phi_\gamma)\right] \Big\} . \qquad (37)
\end{aligned}
$$

In this expression we have designated the product of an asymmetry and $d\sigma_0$ with a caret, so that $\hat{A} = A d\sigma_0$. These products are referred to as profile functions in Refs. [1, 11]. One can of course pull a common factor of $d\sigma_0$ out in front of the above expression, in which case all the profile functions are replaced by their corresponding asymmetries. However, we keep the above form since it is the profile functions that are most simply determined by the CGLN amplitudes. (The definition of each of these profile functions in terms of measurable quantities is given by Appendix B.) The second, third and fourth terms ($\hat{\Sigma}$, $\hat{T}$, $\hat{P}$) are commonly referred to as single-polarization observables, since their leading coefficients contain only a single polarization vector. The subsequent 12 terms are grouped into 3 sets of 4, BT, BR and TR, after the combination of polarization vectors appearing in their leading coefficients. Two of the leading terms have negative coefficients. The first arises because we have taken for the numerator of the beam asymmetry (Σ) the somewhat more common definition of $(\sigma_\perp - \sigma_\parallel)$, rather than the other way around. [Here $\perp$ ($\parallel$) corresponds to $\vec{P}^\gamma_L = \hat{y}$ ($\vec{P}^\gamma_L = \hat{x}$) in the left panel of Fig. 2.] For the second, because of its connection to spin sum rules the numerator of the E asymmetry is often defined in terms of the difference between cross sections with anti-parallel and parallel photon and target spin alignments, respectively [18]. The specific measurements needed to construct each of these observables is tabulated in Appendix B.

Recoil observables are generally specified in the rotated coordinate system with $\hat{z}' = +\hat{k}$. Occasionally, a particular recoil observable will have a more transparent interpretation in the unprimed coordinate system of Fig. 2 [19]. Since a baryon polarization transforms as a standard three vector, the *unprimed* and *primed* observables are simply related:

$$A_x = +A_{x'} \cos\theta_K + A_{z'} \sin\theta_K, \tag{38}$$

$$A_z = -A_{x'} \sin\theta_K + A_{z'} \cos\theta_K, \tag{39}$$

where A represents any one of the BR or TR observables.

It is convenient to arrange the observables entering the general cross section in tabular form, as in Table II. The 4 rows correspond to different states of beam polarization, either without regard to incident polarization (*unpolarized*) or in one the three standard *Stokes* conditions that characterize an ensemble of photons, linear with a $\sin(2\phi_\gamma)$ dependence relative to the reaction plane, linear with a $\cos(2\phi_\gamma)$ dependence, or circular. The columns of the table give the polarization of the target, recoil, or target + recoil combination. One can readily construct from this table the terms that enter the general cross section for any given combination of polarization conditions. For example, with linear beam polarization in or perpendicular to the reaction plane, a longitudinally polarized target (along $\hat{z}$) and an analysis of recoil polarization along the meson (kaon) momentum ($\hat{z}'$), the general cross section is given by the terms in the first (*unpolarized*) and third rows that are either independent of target and recoil polarization ($d\sigma_0$,$-\Sigma$) or in columns associated with polarization along $\hat{z}$ and/or $\hat{z}'$, namely $(1/2)\{[d\sigma_0 + P^T_z P^R_{z'} \hat{L}_{z'}] + P^\gamma_L \cos(2\phi_\gamma)[-\hat{\Sigma} - P^T_z P^R_{z'} \hat{T}_{x'}]\}$.

V. RECOIL POLARIZATION

The above expression in Eq. (37) displays a level of symmetry in the three polarization vectors, $\vec{P}^\gamma$, $\vec{P}^T$ and $\vec{P}^R$. However, while the first two are parameters that are under ex-

TABLE II: Polarization observables in pseudoscalar meson photoproduction. Each observable appears twice in the table. The 16 entries in black indicate the leading polarization dependence of each observable to the general cross section. The three underlined entries in red ($\hat{P}$, $\hat{T}$, $\hat{\Sigma}$) are nominal *single-polarization* quantities that can be measured with double-polarization. Those in bold blue are the unpolarized cross section and 12 nominal double-polarization quantities that can be measured with triple-polarization.

Beam (P^γ)	Target (P^T)			Recoil (P^R)			Target (P^T) + Recoil (P^R)								
				x'	y'	z'	x'	x'	x'	y'	y'	y'	z'	z'	z'
	x	y	z				x	y	z	x	y	z	x	y	z
unpolarized $d\sigma_0$		$\hat{T}$			$\hat{P}$		$\hat{T}_{x'}$		$\hat{L}_{x'}$		$\underline{\hat{\Sigma}}$		$\hat{T}_{z'}$		$\hat{L}_{z'}$
$P_L^\gamma \sin(2\phi_\gamma)$	$\hat{H}$		$\hat{G}$	$\hat{O}_{x'}$		$\hat{O}_{z'}$		$\mathbf{\hat{C}_{z'}}$		$\mathbf{\hat{E}}$		$\mathbf{\hat{F}}$		$\mathbf{-\hat{C}_{x'}}$	
$P_L^\gamma \cos(2\phi_\gamma)$ $-\hat{\Sigma}$		$\underline{-\hat{P}}$			$\underline{-\hat{T}}$		$\mathbf{-\hat{L}_{z'}}$		$\mathbf{\hat{T}_{z'}}$		$\mathbf{-d\sigma_0}$		$\mathbf{\hat{L}_{x'}}$		$\mathbf{-\hat{T}_{x'}}$
circular P_c^γ	$\hat{F}$		$-\hat{E}$	$\hat{C}_{x'}$		$\hat{C}_{z'}$		$\mathbf{-\hat{O}_{z'}}$		$\mathbf{\hat{G}}$		$\mathbf{-\hat{H}}$		$\mathbf{\hat{O}_{x'}}$	

perimental control, the recoil polarization is not. Rather, $\vec{P}^R$ is a byproduct of the angular momentum brought into the entrance channel through $\vec{P}^\gamma$ and $\vec{P}^T$, and the reaction physics. The relations determining $\vec{P}^R$ are readily derived. We start by regrouping terms in the general cross section expression to display the explicit dependence on $\vec{P}^R$ and recast Eq. (37) as,

$$d\sigma_{\mathrm{B,T,R}}(\vec{P}^\gamma, \vec{P}^T, \vec{P}^R) = \frac{1}{2}\left[A^0 + (P^R_{x'})A^{x'} + (P^R_{y'})A^{y'} + (P^R_{z'})A^{z'}\right], \tag{40}$$

where

$$\begin{aligned} A^0 \;=\; & d\sigma_0 - P_L^\gamma \cos(2\phi_\gamma)\hat{\Sigma} + P_y^T \hat{T} \\ & - P_L^\gamma P_y^T \cos(2\phi_\gamma)\hat{P} - P_c^\gamma P_z^T \hat{E} + P_L^\gamma P_z^T \sin(2\phi_\gamma)\hat{G} + P_c^\gamma P_x^T \hat{F} + P_L^\gamma P_x^T \sin(2\phi_\gamma)\hat{H}, \end{aligned}$$

$$\begin{aligned} A^{x'} \;=\; & P_c^\gamma \hat{C}_{x'} + P_L^\gamma \sin(2\phi_\gamma)\hat{O}_{x'} + P_z^T \hat{L}_{x'} + P_x^T \hat{T}_{x'} \\ & + P_L^\gamma P_y^T \sin(2\phi_\gamma)\hat{C}_{z'} - P_c^\gamma P_y^T \hat{O}_{z'} - P_L^\gamma P_x^T \cos(2\phi_\gamma)\hat{L}_{z'} + P_L^\gamma P_z^T \cos(2\phi_\gamma)\hat{T}_{z'}, \end{aligned}$$

$$\begin{aligned} A^{y'} \;=\; & \hat{P} + P_y^T \hat{\Sigma} - P_L^\gamma \cos(2\phi_\gamma)\hat{T} \\ & - P_L^\gamma P_y^T \cos(2\phi_\gamma) d\sigma_0 + P_L^\gamma P_x^T \sin(2\phi_\gamma)\hat{E} + P_c^\gamma P_x^T \hat{G} + P_L^\gamma P_z^T \sin(2\phi_\gamma)\hat{F} - P_c^\gamma P_z^T \hat{H}, \end{aligned}$$

$$
\begin{aligned}
A^{z'} \;=\; & P_c^\gamma \hat{C}_{z'} + P_L^\gamma \sin(2\phi_\gamma)\hat{O}_{z'} + P_z^T \hat{L}_{z'} + P_x^T \hat{T}_{z'} \\
& - P_L^\gamma P_y^T \sin(2\phi_\gamma)\hat{C}_{x'} + P_c^\gamma P_y^T \hat{O}_{x'} + P_L^\gamma P_x^T \cos(2\phi_\gamma)\hat{L}_{x'} - P_L^\gamma P_z^T \cos(2\phi_\gamma)\hat{T}_{x'}.
\end{aligned}
$$

The recoil polarization $\vec{P}^R$ can be resolved as the vector sum of three component vectors, $P_{x'}^R \hat{x}'$, $P_{y'}^R \hat{y}'$, $P_{z'}^R \hat{z}'$. Considering first $P_{x'}^R \hat{x}'$, this is the degree of polarization along $\hat{x}'$ and is given by

$$
P_{x'}^R = \mathfrak{p}_{x',+}^R - \mathfrak{p}_{x',-}^R, \tag{41}
$$

where $\mathfrak{p}_{x',\pm}^R$ is the probability for observing the recoil with spin along $\pm\hat{x}' \equiv (\pm 1, 0, 0)'$. Using Eq. (40), we evaluate this as the ratio of cross sections,

$$
P_{x'}^R = \frac{d\sigma_{\mathrm{B,T,R}}(\vec{P}^\gamma, \vec{P}^T, +1\hat{x}') - d\sigma_{\mathrm{B,T,R}}(\vec{P}^\gamma, \vec{P}^T, -1\hat{x}')}{d\sigma_{\mathrm{B,T,R}}(\vec{P}^\gamma, \vec{P}^T, +1\hat{x}') + d\sigma_{\mathrm{B,T,R}}(\vec{P}^\gamma, \vec{P}^T, -1\hat{x}')} = \frac{A^{x'}}{A^0}. \tag{42}
$$

The $\hat{y}'$ and $\hat{z}'$ recoil components are evaluated in a similar manner. Thus, the components of the recoil polarization are determined from Eq. (40), in terms of combinations of the profile functions and initial polarizations, as

$$
P_{x'}^R = \frac{A^{x'}}{A^0}, \qquad P_{y'}^R = \frac{A^{y'}}{A^0}, \qquad P_{z'}^R = \frac{A^{z'}}{A^0}. \tag{43}
$$

These recoil components determine the orientation of the recoil vector, $\vec{P}^R$, and its magnitude,

$$
|\vec{P}^R| = \frac{1}{A^0}\sqrt{(A^{x'})^2 + (A^{y'})^2 + (A^{z'})^2}. \tag{44}
$$

It is worth clarifying the relationship between Eqs. (37) or (40) and Eq. (43). Equations (37) and (40) display the general dependence of the cross section upon the three polarization vectors, each of which is in a superposition of two spin states. If any one polarization is not observed, either by not experimentally preparing it ($\vec{P}^\gamma$ or $\vec{P}^T$) or by not detecting it ($\vec{P}^R$), then the terms proportional to that polarization average or sum to zero and drop out of the cross section. The action of preparing or detecting a polarization forces the corresponding magnetic substate population into a particular distribution, which in the case of the recoil polarization is given by Eq. (43). A particular consequence of this is that one may not substitute Eq. (43) back into Eq. (40) to obtain a cross section that appears to be independent of recoil polarization.

An expression similar in spirit to Eq. (40) but different in form is given by Adelseck and Saghai in Ref. [10]. However, there is at least one obvious misprint, with two terms involving P_z^R and O_z but none with P_z^R and O_x.

In practice, the recoil polarization is measured either following a secondary scattering or, in the case of hyperon channels, through the angular distribution of their weak decays. $K\Lambda \to K\pi^- p$ production provides a particularly efficient channel for recoil measurements. In the rest frame of the decaying Λ, the angular distribution of the decay proton follows $(1/2)[1 + \alpha|\vec{P}^\Lambda|\cos(\Theta_p)]$, where Θ_p is the angle between the proton momentum and the lambda polarization direction [20]. Since the analyzing power in this decay is quite high, $\alpha = 0.642 \pm 0.013$ [21], recoil measurements in modern quasi 4π detectors can be carried out without significant penalty in statistics. Such measurements then provide information on combinations of observables through Eq. (43). It is instructive to consider a few examples.

1. Unpolarized beam and target, $P^\gamma_{L,c} = P^T = 0$: Then $A^0 = d\sigma_0$, $A^{x'} = 0$, $A^{y'} = \hat{P}$ and $A^{z'} = 0$, so that

$$\vec{P}^R = (0, P = \hat{P}/d\sigma_0, 0). \tag{45}$$

   Thus, even when the initial state is completely unpolarized, a measured recoil polarization will be perpendicular to the reaction plane.

2. Unpolarized beam and longitudinally polarized target, $P^\gamma_{L,c} = 0$ and $\vec{P}^T = (0, 0, P^T_z)$: Then $A^0 = d\sigma_0$, $A^{x'} = P^T_z \hat{L}_{x'}$, $A^{y'} = \hat{P}$, and $A^{z'} = P^T_z \hat{L}_{z'}$, so that

$$\vec{P}^R = (P^T_z L_{x'}, P, P^T_z L_{z'}). \tag{46}$$

   Thus a measurement of the components of the recoil polarization determine the $L_{x'}$, P and $L_{z'}$ asymmetries.

3. Circularly polarized beam (P^γ_c) and unpolarized target ($P^T = 0$): Then $A^0 = d\sigma_0$, $A^{x'} = P^\gamma_c \hat{C}_{x'}$, $A^{y'} = \hat{P}$, and $A^{z'} = P^\gamma_c \hat{C}_{z'}$, so that

$$\vec{P}^R = (P^\gamma_c C_{x'}, P, P^\gamma_c C_{z'}). \tag{47}$$

   This is the form assumed in the analysis of the CLAS-g1c data in Ref. [19].

4. Linearly polarized beam (P^γ_L) and unpolarized target ($P^T = 0$): Then $A^0 = d\sigma_0 - P^\gamma_L \cos(2\phi_\gamma)\hat{\Sigma}$, $A^{x'} = P^\gamma_L \sin(2\phi_\gamma)\hat{O}_{x'}$, $A^{y'} = \hat{P} - P^\gamma_L \cos(2\phi_\gamma)\hat{T}$, and $A^{z'} = P^\gamma_L \sin(2\phi_\gamma)\hat{O}_{z'}$, so that

$$\vec{P}^R = \left(\frac{P^\gamma_L \sin(2\phi_\gamma) O_{x'}}{1 - P^\gamma_L \cos(2\phi_\gamma)\Sigma}, \frac{P - P^\gamma_L \cos(2\phi_\gamma) T}{1 - P^\gamma_L \cos(2\phi_\gamma)\Sigma}, \frac{P^\gamma_L \sin(2\phi_\gamma) O_{z'}}{1 - P^\gamma_L \cos(2\phi_\gamma)\Sigma} \right), \tag{48}$$

   which is the form assumed in the analysis of the GRAAL data in Ref. [5].

5. Circularly polarized beam (P_c^γ) and longitudinally polarized target [$\vec{P}^T = (0, 0, P_z^T)$]: Then $A^0 = d\sigma_0 - P_c^\gamma P_z^T \hat{E}$, $A^{x'} = P_c^\gamma \hat{C}_{x'} + P_z^T \hat{L}_{x'}$, $A^{y'} = \hat{P} - P_c^\gamma P_z^T \hat{H}$, and $A^{z'} = P_c^\gamma \hat{C}_{z'} + P_z^T \hat{L}_{z'}$, so that

$$\vec{P}^R = \left(\frac{P_c^\gamma C_{x'} + P_z^T L_{x'}}{1 - P_c^\gamma P_z^T E}, \frac{P - P_c^\gamma P_z^T H}{1 - P_c^\gamma P_z^T E}, \frac{P_c^\gamma C_{z'} + P_z^T L_{z'}}{1 - P_c^\gamma P_z^T E} \right). \tag{49}$$

Here, kinematically and spin complete measurements provide the greatest flexibility. An initial beam-target analysis summing over final states (i.e., ignoring the recoil) results in the cross section A^0, which determines the E asymmetry and hence the denominator in Eq. (49). With an analysis, averaging over initial target polarizations $\pm P_z^T$, measurements of the recoil polarization vector then determine the $C_{x'}$, P and $C_{z'}$ asymmetries. Another pass through the data, averaging instead over initial beam polarization states, $\pm P_c^\gamma$, and with an analysis of the $P_{x'}^R$ and $P_{z'}^R$ recoil components, gives the $L_{x'}$ and $L_{z'}$ asymmetries. Finally, by keeping track of both beam and target polarization states, a measurement of the $P_{y'}^R$ recoil component gives the H asymmetry. Although the uncertainty in this determination of H will include the propagation of errors from P and E, this is expected to be held to a reasonable level in the modern set of experiments that are now under way. The significance of this determination is that it has not required the use of a transversely polarized target, as would otherwise be required by the leading polarization dependence of it in Eq. (37). In general, the latter would require a completely separate experiment with different systematics.

6. Linearly polarized beam (P_L^γ) and longitudinally polarized target [$\vec{P}^T = (0, 0, P_z^T)$]: Then $A^0 = d\sigma_0 - P_L^\gamma \cos(2\phi_\gamma)\hat{\Sigma} + P_L^\gamma P_z^T \sin(2\phi_\gamma)\hat{G}$, $A^{x'} = P_L^\gamma \sin(2\phi_\gamma)\hat{O}_{x'} + P_z^T \hat{L}_{x'} + P_L^\gamma P_z^T \cos(2\phi_\gamma)\hat{T}_{z'}$, $A^{y'} = \hat{P} - P_L^\gamma \cos(2\phi_\gamma)\hat{T} + P_L^\gamma P_z^T \sin(2\phi_\gamma)\hat{F}$, and $A^{z'} = P_L^\gamma \sin(2\phi_\gamma)\hat{O}_{z'} + P_z^T \hat{L}_{z'} - P_L^\gamma P_z^T \cos(2\phi_\gamma)\hat{T}_{x'}$, so that

$$\begin{aligned} \vec{P}^R = \Bigg(& \frac{P_L^\gamma \sin(2\phi_\gamma) O_{x'} + P_z^T L_{x'} + P_L^\gamma P_z^T \cos(2\phi_\gamma) T_{z'}}{1 - P_L^\gamma \cos(2\phi_\gamma)\Sigma + P_L^\gamma P_z^T \sin(2\phi_\gamma) G}, \\ & \frac{P - P_L^\gamma \cos(2\phi_\gamma) T + P_L^\gamma P_z^T \sin(2\phi_\gamma) F}{1 - P_L^\gamma \cos(2\phi_\gamma)\Sigma + P_L^\gamma P_z^T \sin(2\phi_\gamma) G}, \\ & \frac{P_L^\gamma \sin(2\phi_\gamma) O_{z'} + P_z^T L_{z'} - P_L^\gamma P_z^T \cos(2\phi_\gamma) T_{x'}}{1 - P_L^\gamma \cos(2\phi_\gamma)\Sigma + P_L^\gamma P_z^T \sin(2\phi_\gamma) G} \Bigg). \end{aligned} \tag{50}$$

With such data a beam-target analysis summing over final states (i.e., ignoring the recoil) determines the cross section A^0, and hence the Σ and G asymmetries from a Fourier analysis of the ϕ_γ dependence. This fixes the denominators in Eq. (50). With another analysis pass, averaging over initial target polarizations, measurements of the recoil polarization vector provide a determination of the $O_{x'}$, P and T, and $O_{z'}$ asymmetries. Another pass through the same data, integrating over ϕ_γ, gives the $L_{x'}$, P and $L_{z'}$ asymmetries from measurements of the recoil polarization vector. Finally, a Fourier analysis of beam polarization states, using the difference between opposing target orientations, $P^T_z - P^T_{-z}$, together with a measurement of recoil polarization allows the separation of $L_{x'}$ and $T_{z'}$, F (which would otherwise require a transversely polarized target), and $L_{z'}$ and $T_{x'}$.

Thus, by judicious use of recoil polarization and a polarized beam, all 16 observables can be determined with a longitudinally polarized target (often in several ways), and in so doing with largely common systematics.

A corresponding set of expressions can be developed for a transversely polarized target, although they are inherently more complicated since, for fixed target polarization perpendicular to $+\hat{z}$, any reaction plane will generally involve both transverse target components P^T_x and P^T_y.

7. Unpolarized beam ($P^\gamma_{L,c} = 0$) with a transversely polarized target and [$\vec{P}^T = (P^T_x, P^T_y, 0)$]: Then $A^0 = d\sigma_0 + P^T_y \hat{T}$, $A^{x'} = P^T_x \hat{T}_{x'}$, $A^{y'} = \hat{P} + P^T_y \hat{\Sigma}$, and $A^{z'} = P^T_x \hat{T}_{z'}$, so that
$$\vec{P}^R = \left(\frac{P^T_x T_{x'}}{1 + P^T_y T}, \frac{P + P^T_y \Sigma}{1 + P^T_y T}, \frac{P^T_x T_{z'}}{1 + P^T_y T} \right). \tag{51}$$
Here an analysis summing over final states (i.e., ignoring the recoil) results in the cross section A^0, and a fit varying P^T_y as the reaction plane tilts relative to the direction of the target polarization determines the T asymmetry. A subsequent analysis of the recoil polarization components then determines $T_{x'}$, P, Σ, and $T_{z'}$.

8. Circularly polarized beam (P^γ_c) and transverse target polarization [$\vec{P}^T = (P^T_x, P^T_y, 0)$]: Then $A^0 = d\sigma_0 + P^T_y \hat{T} + P^\gamma_c P^T_x \hat{F}$, $A^{x'} = P^\gamma_c \hat{C}_{x'} + P^T_x \hat{T}_{x'} - P^\gamma_c P^T_y \hat{O}_{z'}$, $A^{y'} = \hat{P} + P^T_y \hat{\Sigma} + P^\gamma_c P^T_x \hat{G}$, and $A^{z'} = P^\gamma_c \hat{C}_{z'} + P^T_x \hat{T}_{z'} + P^\gamma_c P^T_y \hat{O}_{x'}$, so that
$$\vec{P}^R = \left(\frac{P^\gamma_c C_{x'} + P^T_x T_{x'} - P^\gamma_c P^T_y O_{z'}}{1 + P^T_y T + P^\gamma_c P^T_x F}, \frac{P + P^T_y \Sigma + P^\gamma_c P^T_x G}{1 + P^T_y T + P^\gamma_c P^T_x F}, \frac{P^\gamma_c C_{z'} + P^T_x T_{z'} + P^\gamma_c P^T_y O_{x'}}{1 + P^T_y T + P^\gamma_c P^T_x F} \right). \tag{52}$$

In this case, a beam-target analysis summing over final states (i.e., ignoring the recoil) results in the cross section A^0 containing the terms in the T and F asymmetries, and these can be separated by first averaging over initial photon states, which removes F. A subsequent analysis, reconstructing the recoil polarization while averaging over initial circular photon states allows one to deduce $T_{x'}$ and $T_{z'}$ from $P^R_{x'}$ and $P^R_{z'}$. Alternatively, with fixed beam polarization and recoil analysis, a fit varying P^T_x and P^T_y as the reaction plane tilts in azimuth relative to the direction of the transversely polarized target determines all of the asymmetries in the numerators of Eq. (52).

We leave it to the reader to write out the final combination of linearly polarized beam and transverse target polarization. There the recoil polarization components involve ratios of 4 to 5 terms each. It remains to be seen if sequential analyses of such data are of practical use, given limitations on statistics.

VI. RELATING OBSERVABLES TO CGLN AMPLITUDES

We are now in a position to use any set of multipole amplitudes to calculate the four CGLN amplitudes from Eqs. (15)-(18) and then with these, evaluate (a) the polarization observables by using the formulae described in the Sec. III and the spin orientations specified in the tables of Appendix B, and (b) the same observables calculated from the analytic expressions, as given in Refs. [10, 11] or Refs. [12, 13]. As expected, the absolute magnitudes from the two methods are the same, but some of their signs are different. In doing so, we are able to fix the signs of the analytic expressions for the experimental conditions specified in Fig. 2 and Appendix B. Our results are:

$$\begin{aligned}
d\sigma_0 &= +\Re e\left\{F_1^*F_1 + F_2^*F_2 + \sin^2\theta(F_3^*F_3/2 + F_4^*F_4/2 + F_2^*F_3 + F_1^*F_4 \right. \\
&\quad \left. + \cos\theta F_3^*F_4) - 2\cos\theta F_1^*F_2\right\}\rho_0, && (53a) \\
\hat{\Sigma} &= -\sin^2\theta\Re e\left\{\left(F_3^*F_3 + F_4^*F_4\right)/2 + F_2^*F_3 + F_1^*F_4 + \cos\theta F_3^*F_4\right\}\rho_0, && (53b) \\
\hat{T} &= +\sin\theta\Im m\left\{F_1^*F_3 - F_2^*F_4 + \cos\theta(F_1^*F_4 - F_2^*F_3) - \sin^2\theta F_3^*F_4\right\}\rho_0, && (53c) \\
\hat{P} &= -\sin\theta\Im m\left\{2F_1^*F_2 + F_1^*F_3 - F_2^*F_4 - \cos\theta(F_2^*F_3 - F_1^*F_4) - \sin^2\theta F_3^*F_4\right\}\rho_0, && (53d) \\
\hat{E} &= +\Re e\left\{F_1^*F_1 + F_2^*F_2 - 2\cos\theta F_1^*F_2 + \sin^2\theta(F_2^*F_3 + F_1^*F_4)\right\}\rho_0, && (53e) \\
\hat{G} &= +\sin^2\theta\Im m\left\{F_2^*F_3 + F_1^*F_4\right\}\rho_0, && (53f) \\
\hat{F} &= +\sin\theta\Re e\left\{F_1^*F_3 - F_2^*F_4 - \cos\theta(F_2^*F_3 - F_1^*F_4)\right\}\rho_0, && (53g) \\
\hat{H} &= -\sin\theta\Im m\left\{2F_1^*F_2 + F_1^*F_3 - F_2^*F_4 + \cos\theta(F_1^*F_4 - F_2^*F_3)\right\}\rho_0, && (53h) \\
\hat{C}_{x'} &= -\sin\theta\Re e\left\{F_1^*F_1 - F_2^*F_2 - F_2^*F_3 + F_1^*F_4 - \cos\theta(F_2^*F_4 - F_1^*F_3)\right\}\rho_0, && (53i) \\
\hat{C}_{z'} &= -\Re e\left\{2F_1^*F_2 - \cos\theta(F_1^*F_1 + F_2^*F_2) + \sin^2\theta(F_1^*F_3 + F_2^*F_4)\right\}\rho_0, && (53j) \\
\hat{O}_{x'} &= -\sin\theta\Im m\left\{F_2^*F_3 - F_1^*F_4 + \cos\theta(F_2^*F_4 - F_1^*F_3)\right\}\rho_0, && (53k) \\
\hat{O}_{z'} &= +\sin^2\theta\Im m\left\{F_1^*F_3 + F_2^*F_4\right\}\rho_0, && (53l) \\
\hat{L}_{x'} &= +\sin\theta\Re e\left\{F_1^*F_1 - F_2^*F_2 - F_2^*F_3 + F_1^*F_4 + \sin^2\theta(F_4^*F_4 - F_3^*F_3)/2 \right. \\
&\quad \left. + \cos\theta(F_1^*F_3 - F_2^*F_4)\right\}\rho_0, && (53m) \\
\hat{L}_{z'} &= +\Re e\left\{2F_1^*F_2 - \cos\theta(F_1^*F_1 + F_2^*F_2) + \sin^2\theta(F_1^*F_3 + F_2^*F_4 + F_3^*F_4) \right. \\
&\quad \left. + \cos\theta\sin^2\theta(F_3^*F_3 + F_4^*F_4)/2\right\}\rho_0, && (53n) \\
\hat{T}_{x'} &= -\sin^2\theta\Re e\left\{F_1^*F_3 + F_2^*F_4 + F_3^*F_4 + \cos\theta(F_3^*F_3 + F_4^*F_4)/2\right\}\rho_0, && (53o) \\
\hat{T}_{z'} &= +\sin\theta\Re e\left\{F_1^*F_4 - F_2^*F_3 + \cos\theta(F_1^*F_3 - F_2^*F_4) \right. \\
&\quad \left. + \sin^2\theta(F_4^*F_4 - F_3^*F_3)/2\right\}\rho_0. && (53p)
\end{aligned}$$

A comparable set of expressions are given by Fasano, Tabakin and Saghai (FTS) in Ref. [11]. That paper defines the photon polarization using Stokes vectors taken from optics where right and left circular polarization are interpreted differently. Nonetheless, they associate photon helicity +1 with what Ref. [11] refers to as r circular polarization. Keeping this convention and allowing for their different definition of the E beam-target asymmetry, the above expressions are consistent with those of Ref. [11].

Comparing the above relations to those given by Knöchlein, Drechsel and Tiator (KDT) (Appendix B and C of Ref. [13]), six have different signs, the BT observable H, the TR observable $L_{x'}$ and all four of the BR observables $C_{x'}$, $C_{z'}$, $O_{x'}$ and $O_{z'}$. The KDT paper [13] is listed in the MAID on-line meson production analysis [22–24] as the defining reference for the connection between CGLN amplitudes and polarization observables. To check if these differences persist in the MAID code we have downloaded MAID multipoles, used the relations in Eqs. (15)-(18) to construct from these the four CGLN F_i amplitudes, and then used our equations (53) above to construct observables. Comparing the results to direct predictions of observables from the MAID code, we find the same six sign differences. However, in the general form of the cross section given by KDT in Ref. [13] these six observables appear with a negative coefficient, as opposed to our form of the cross section in Eq. (37). This is equivalent to interchanging the σ_1 and σ_2 measurements of Appendix B that are needed to construct these six observables. The choice of these two measurements that we list in Appendix B seem the obvious ones. They are, with the exception of the E asymmetry, the same choices used by FTS in Ref. [11]. Despite the fact that KDT refer to their definition of observables as *common* to FTS in Ref. [11], there is evidently a sign difference for H, $L_{x'}$, $C_{x'}$, $C_{z'}$, $O_{x'}$ and $O_{z'}$.

We have conducted a similar test with the GWU/VPI SAID on-line analysis code [25, 26], downloading SAID multipoles, using the relations in Eqs. (15)-(18) to construct from these the four CGLN F_i amplitudes, and then using our equations (53) above to construct observables. When the results are compared to direct predictions of observables from the SAID code, again the same 6 observables (H, $L_{x'}$, $C_{x'}$, $C_{z'}$, $O_{x'}$, $O_{z'}$) differ in sign. For the definition of observables, SAID refers to the Barker, Donnachie and Storrow paper [7]. In general, the discussion in that paper tends to be too condensed to definitively address signs, but at least in the cases of H, $O_{x'}$ and $O_{z'}$ they define the required (B,T,R) measurements as $\{L(\pm\pi/4), x, -\}$, $\{L(\pm\pi/4), -, x'\}$ and $\{L(\pm\pi/4), -, z'\}$, respectively. These appear to be in agreement with our definitions in Appendix B, which forces us to conclude that the SAID choice of signs used to construct these six observables from amplitudes is inconsistent with the assumed definitions of the measurements needed to construct these asymmetries.

We have repeated this same test with the Bonn-Gatchina (BoGa) on-line PWA [27], downloading BoGa multipoles, using the relations of Eqs. (15)-(18) to construct the four CGLN amplitudes, and then using our Eqs. (53) to construct observables. Comparing these to direct predictions of observables from the BoGa code, the results are identical, except for the E asymmetry which is of opposite sign. However, for the definition of observables the BoGa on-line site refers to FTS of Ref. [11], whose definitions are the same as in our Appendix B except for a sign change in the E asymmetry. Thus, we conclude that the relations between observables and amplitudes used in the BoGa analysis is completely consistent with the present work.

New data are emerging from the current generation of polarization experiments which make these sign differences an important issue. In Ref. [19], recent results for the $C_{x'}$ and $C_{z'}$ asymmetries have been compared with the direct predictions of the Kaon-MAID code, ignoring the sign reversal. This has particularly dramatic consequences for the BR asymmetry $C_{z'}$ which is constrained by angular momentum conservation to the value of $+1$ at $\theta_K = 0$. This is straightforward to see from Appendix B, where $C_{z'} = \{\sigma_1(+1, 0, +z') - \sigma_2(+1, 0, -z')\}/\{\sigma_1 + \sigma_2\}$. When the incident photon spin is oriented along $+\hat{z}$, only those target nucleons with anti-parallel spin can contribute to the production of spin zero mesons at $\theta_K = 0$, and the projection of the total angular momentum along $\hat{z}$ is $+\frac{1}{2}$. Thus, the recoil baryon must have its spin oriented along $+\hat{z} = +\hat{z}'$ at $\theta_K = 0$, so that σ_2 must vanish. The recent measurements on $K^+\Lambda$ production [19] clearly show this asymmetry approaching $+1$ at $\theta_K = 0$, along with MAID predictions approaching -1.

The trends in $C_{x'}$ and $C_{z'}$ for $\gamma p \to K^+\Lambda$ are illustrated with two energies in Fig. 3. The data (green circles) are recent CLAS-g1c results from Ref. [19] and these are compared to the direct predictions from Kaon-MAID (black, dashed), SAID (black, dotted) and BoGa (blue, dot-dashed) codes. The MAID and SAID predictions clearly have the wrong limits for $C_{z'}$ at 0 and 180 degrees. Also shown are predictions using the multipoles of Juliá-Díaz, Saghai, Lee and Tabakin (JSLT) from Ref. [28], passed through our expressions to construct observables (solid blue curves). The MAID and SAID sign differences are also evident in $C_{x'}$, particularly at low energies where only a few partial waves are contributing - top panels of Fig. 3. There it is clear that the predictions of the different partial solutions are essentially very similar, differing only in sign.

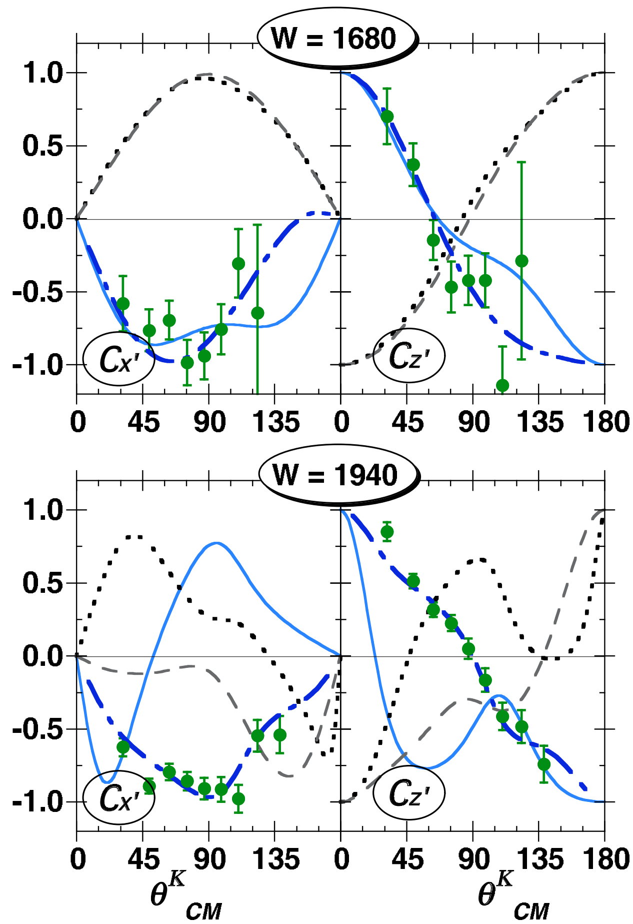

FIG. 3: (Color online) $C_{x'}$ (left) and $C_{z'}$ (right) for the $\gamma p \to K^+\Lambda$ reaction at $W = 1680$ MeV (top) and $W = 1940$ MeV (bottom). Kaon-MAID predictions are dashed (black) [22–24], SAID predictions are dotted (black) [25, 26], BoGa predictions are dot-dashed (blue) [27] and predictions from JSLT [28] are solid (blue). The green circles are from Ref. [19].

VII. RELATIONS BETWEEN OBSERVABLES

Since photo-production is characterized by 4 complex amplitudes, Eq. (9), the 16 observables of Eq. (53) are not independent. There are in fact many relations between them. The profile functions of Eq. (53) are bilinear products of the CGLN amplitudes, and one of the more complete sets of equalities interrelating them has been derived by Chiang and Tabakin from the Fierz identities that relate bilinear products of currents [1]. Such relations are particularly useful, since they allow the comparison of data on one observable with an evaluation in terms of products of other observables. Any determination of the amplitude will invariably require combining data on different polarization observables which in general come from different experiments, each having different systematic scale uncertainties. The Fierz identities provide a means of enforcing consistency. As a practical example, in the next section we use two of the identities in a multipole analysis to fix the scales of different data sets in a fit weighted by their systematic errors.

We have numerically checked the 37 Fierz identities of Ref. [1]. Many required revisions in signs. A corrected set is listed in the first three sections of Appendix C. Another set of relations has been given by Artru, Richard and Soffer (ARS) [29, 30]. These are different in form but can be derived from our Fierz identities, although with some differences in signs. A consistent set is listed in Appendix C 4.

In addition to identities, there are a number of inequalities, such as $(P)^2+(C_{x'})^2+(C_{z'})^2 \leq 1$, which are often referred to as positivity constraints [29]. These involve the sums of the squares of asymmetries, and as such are immune to sign issues. They can be particularly useful when extracting sets of asymmetries from fits to experimental data [31], as in the examples discussed in Sec. V. But since our focus here is amplitude reduction from cross sections and asymmetries, we defer the reader to a recent review of such inequalities [30].

VIII. MULTIPOLE ANALYSES

The ultimate goal of the new generation of experiments now under way is a complete experimental determination of the multipole decomposition of the full amplitude in pseudoscalar meson production. While the data published to date is still insufficient to satisfy the Chiang and Tabakin requirements for removing ambiguities [1], it is instructive to outline the process and examine the impact of recently published polarization measurements. We focus here on the $\gamma p \to K^+\Lambda$ channel, which so far has provided the largest number of different observables.

To avoid bias, the first stage in any multipole decomposition is a single-energy analysis, one beam/W energy at a time without any assumptions on energy-dependent behavior. The range of recent published $K^+\Lambda$ measurements is summarized in Table III. [Cross section data from the SAPHIR detector at Bonn [32] have an appreciable (20%) angle- and energy-dependent difference from the CLAS experiments. This level of incompatibility makes it impossible to include them in the present analyses.] While some of the data sets span the full nucleon resonance region in extremely fine steps, single-energy analyses are limited by the observables with the coarsest granularity, which in this case are the $C_{x'}$, $C_{z'}$ measurements (data group 3 [19]). The only published $O_{x'}$, $O_{z'}$ and T data are from GRAAL (data groups 5 and 8 [5]). The combination of these data sets allows us to combine groups 1-8 at 5 different beam energies, with roughly 100 MeV steps in beam energy, for which 8 different observables are now available.

A. Coordinate Transformations

There are several different choices for coordinate systems in use and before data from the different experiments can be combined in a common analysis we transformed them to the system defined in Fig. 2. The beam-recoil data of group 3 [19] were reported in unprimed laboratory coordinates. These are related to the primed system of Fig. 2 by the inverse relations of Eqs. (38)-(39),

$$\begin{aligned} C_{x'} &= C_x \cos\theta_K - C_z \sin\theta_K, \\ C_{z'} &= C_x \sin\theta_K + C_z \cos\theta_K. \end{aligned} \tag{54}$$

The GRAAL papers use the coordinates of Adelseck and Saghai [10]. Relative to $\hat{y}' = \hat{y}$, their $\hat{x}$ and $\hat{z}$ axes are reversed from those of Fig. 2, so that Σ, T and P are unchanged in transferring to our coordinated, but $O_{x',z'}$ are the negative of what they refer to as $O_{x,z}$, so that

$$O_{x',z'} = -O^{\mathrm{GRAAL}}_{x,z}. \tag{55}$$

B. Constraining Systematic scale uncertainties

Each experiment has reported systematic errors that reflect an uncertainty in the scale of the entire data set, as a group. We use a fairly standard procedure of imposing self-consistence within a collection of data sets by including their measurement scales as parameters in a fit minimizing χ^2 [36]. To fix first the scales of the polarization observables, data groups (2,3,5,6,7,8) of Table III, we use the Fierz identities (L.BR) and (S.br) of Appendix C to construct the quantities,

$$\begin{aligned} F_{\mathrm{L.BR}} &= \Sigma P - C_{x'} O_{z'} + C_{z'} O_{x'} - T, \\ F_{\mathrm{S.br}} &= O^2_{x'} + O^2_{z'} + C^2_{x'} + C^2_{z'} + \Sigma^2 - T^2 + P^2 - 1, \end{aligned} \tag{56}$$

TABLE III: Summary of recent published results on $K^+\Lambda$ photoproduction. (Systematic uncertainties on the CLAS data are taken from the indicated references. The systematic errors on the GRAAL measurements reflect their reported uncertainty in beam polarization, in the assumed weak-Λ-decay parameter and in the resulting error propagation through the extraction of $O_{x'}$, $O_{z'}$ and T.)

Data group	Experiment	Observables	E_γ range (MeV) W range (MeV)	$\Delta E_\gamma/\Delta W$ binning	Systematic scale error
1	CLAS-g11a [33]	$d\sigma_0$	938-3814		±8%
			1625-2835	10	(E_γ dependent)
2	CLAS-g11a [33]	P	938-3814		±0.05
			1625-2835	10	
3	CLAS-g1c [19]	$C_{x'}$, $C_{z'}$	1032-2741	101	±0.03
			1679-2454		
4	CLAS-g1c [34]	$d\sigma_0$	944-2950	25	±8%
			1628-2533		(E_γ dependent)
5	GRAAL [5]	$O_{x'}$, $O_{z'}$	980-1466	50	±4%
			1649-1906		
6	GRAAL [4]	P	980-1466	50	±3%
			1649-1906		
7	GRAAL [4]	Σ	980-1466	50	±2%
			1649-1906		
8	GRAAL [5]	T	980-1466	50	±5%
			1649-1906		
9	LEPS [35]	Σ	1550-2350	100	±3%
			1947-2300		

both of which have the expectation value of 0 at each angle and energy. Our fitting procedure then minimizes the χ^2 function,

$$\chi^2 = \sum_{E_\gamma}\sum_{\theta_K}\left\{\left[\frac{F_{\mathrm{L.BR}}(f_i x_{i\theta}^{\mathrm{exp}})}{\delta F_{\mathrm{L.BR}}(f_i\sigma_{x_{i\theta}})}\right]^2_{i=2,3,5,6,7,8} + \left[\frac{F_{\mathrm{S.br}}(f_i x_{i\theta}^{\mathrm{exp}})}{\delta F_{\mathrm{S.br}}(f_i\sigma_{x_{i\theta}})}\right]^2_{i=2,3,5,6,7,8}\right\} + \sum_i\left[\frac{f_i-1}{\sigma_{f_i}}\right]^2, \tag{57}$$

TABLE IV: Fitted scales for the data sets of Table III that are used to construct the relations in Eq. (57).

Data group	Experiment	Observables	Fitted scale (f_i)	Scale error (σ_{f_i})
2	CLAS-g11a	P	1.000	0.049
3	CLAS-g1c	$C_{x'}$, $C_{z'}$	0.984	0.025
5	GRAAL	$O_{x'}$, $O_{z'}$	0.997	0.035
6	GRAAL	P	1.001	0.030
7	GRAAL	Σ	1.001	0.020
8	GRAAL	T	0.992	0.040

where the index $i \equiv (2, 3, 5, 6, 7, 8)$ runs through each of the data groups of asymmetries ($x_{i\theta}^{\text{exp.}}$) needed to construct the Fierz relations of (56). All data from a set i having a systematic scale error (σ_{f_i}) are multiplied by a common factor (f_i) while adding $(f_i - 1)^2/\sigma_{f_i}^2$ to the χ^2. This last term weights the penalty for choosing a normalization scale different from unity by the reported systematic uncertainty of the experiment.

In this procedure polynomial fits are used, where needed, to interpolate the data of Table III to a common angle and energy. There are two measurements of the recoil polarization asymmetry (P), from groups 2 and 6 in Table III, and a weighted mean of these data, including their scale factors, is used in evaluating Eq. (57). The scale factors resulting from this fit are listed in Table IV. All are close to unity. The resulting evaluations of the Fierz relation, using the scaled data, are shown in Fig. 4.

While the results in Fig. 4 scatter around zero as expected, the fluctuations are sometimes appreciable. These cannot readily be removed with an energy- and angle-independent scale factor. It is likely this results from combining data from different detectors. While global uncertainties such as flux normalization and target thickness can be readily estimated and easily fitted away in this type of procedure, angle-dependent variations in detector efficiencies tend to be the most problematic to control and quantify.

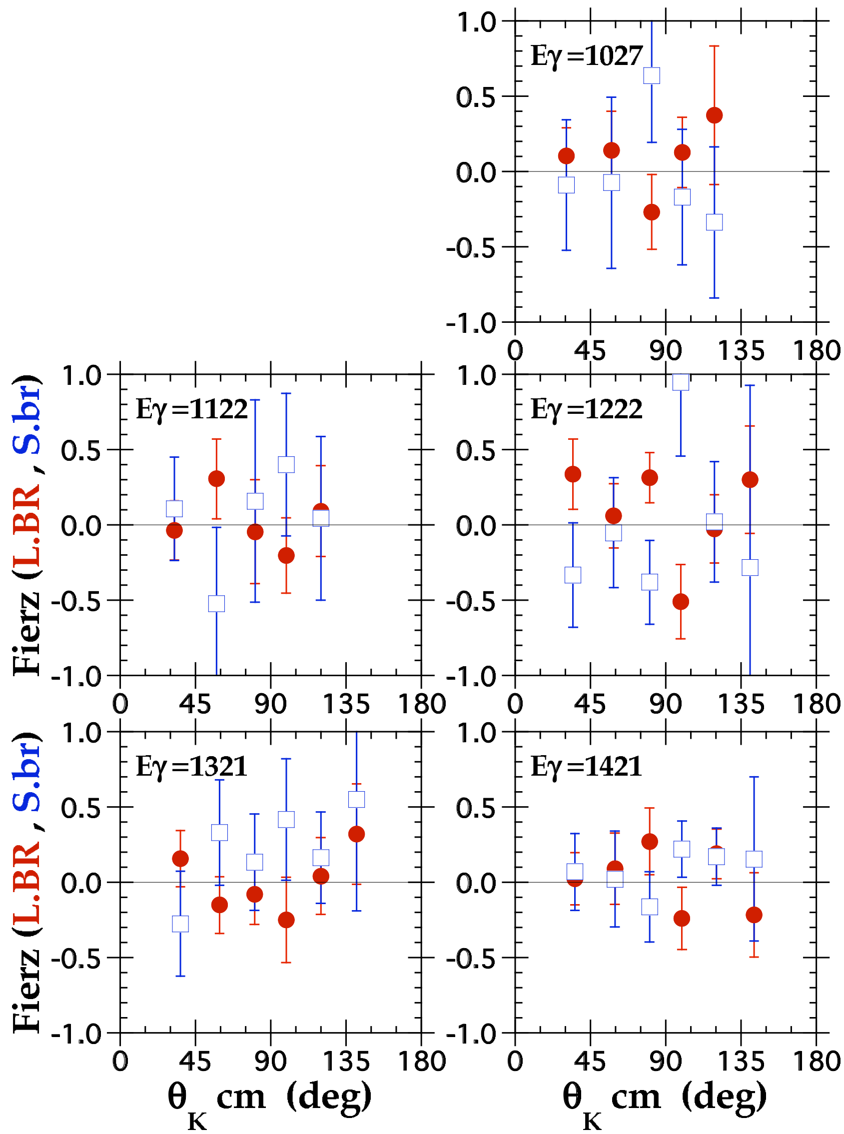

FIG. 4: (Color online) Evaluations of the two Fierz relations (L.BR) (solid red circles) and (S.br) (open blue squares) of Eq. (56), using the data of Table III and the fitted scales of Table IV.

C. Multipole fitting procedure

The observables of Table III are determined by the CGLN amplitudes through Eq. (53), and these are in turn determined by the multipoles through Eqs. (15)-(18). Since the multipoles are reduced matrix elements and independent of angle, fitting them directly allows the use of complete angular distributions for each observable. We fix the scales (f_i) of the polarization observables (Σ, T, P, $C_{x'}$, $C_{z'}$, $O_{x'}$, $O_{z'}$) to their fitted values in Table IV, and now vary the multipoles, as well as the scales f_1 and f_4 for the unpolarized cross section

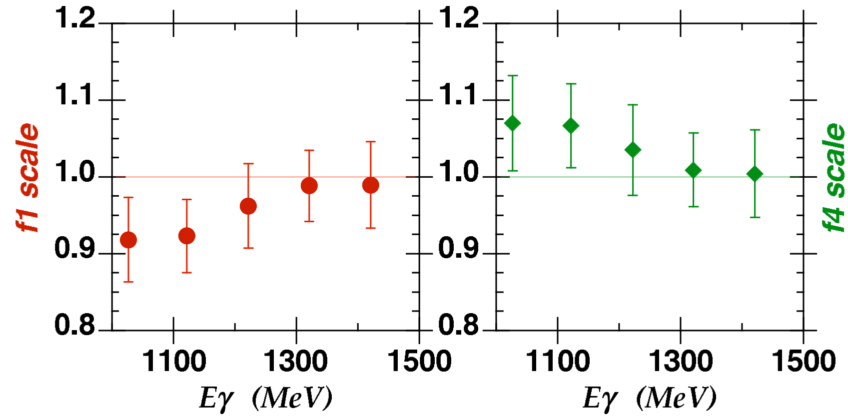

FIG. 5: (Color online) Fitted scales for the cross section ($d\sigma_0$) measurements of Ref. [33], f_1 as red circles, and Ref. [34], f_4 as green diamonds.

($d\sigma_0$) measurements (groups 1 and 4 in Table III) to minimize the χ^2 function,

$$\chi^2 = \sum_{i=1}^{N_s} \left\{ \sum_{j=1}^{N_i} \left[\frac{f_i x_{ij}^{\text{exp}} - x_{ij}^{\text{fit}}(\vec{\zeta})}{f_i \sigma_{x_{ij}}} \right]^2 \right\} + \sum_{i=1,4} \left[\frac{f_i - 1}{\sigma_{f_i}} \right]^2 , \tag{58}$$

where N_s is the number of independent data sets, each having N_i points. x_{ij}^{exp} and $\sigma_{x_{ij}}$ are the j-th experimental datum from the i-th data set and its associated measurement error, respectively, $x_{ij}^{\text{fit}}(\vec{\zeta})$ is the value predicted from the $\vec{\zeta}$ multipole set being fit, and f_i is the global scale parameter associated with the i-th data set. As before, the last term weights the penalty for choosing a cross section scale different from unity by the reported systematic uncertainties for data groups 1 and 4 [36].

Thus our fitting procedure is a two-step process, first minimizing Eq. (57) by varying the scale factors of the polarization data, and then minimizing Eq. (58) in a second step by varying the multipoles and the cross section scales. These two cannot be combined into a single step in which Fierz relations such as Eq. (56) are minimized by varying multipoles, since all properly constructed multipoles will automatically satisfy the Fierz identities.

While the cross section experiments report the global systematic uncertainties listed in Table III, comparisons given in Ref. [33] show a clear energy dependence to the scale difference between them, which is most pronounced at low energies. Accordingly, we have fitted separate cross section scales at each energy and the results are plotted in Fig. 5.

Cross sections for any reaction generally fall with increasing angular momentum, which guarantees the ultimate convergence of a multipole expansion. However, in practice such expansions must be truncated to limit the maximum angular momentum to a value that is essentially determined by the statistical precision and breadth of kinematic coverage of the data sets. The ultimate goal of such work will be the identification of the excited states of the nucleon, and this will require, as a minimum, accurate multipole information up to at least $L = 2$ to be useful. As has been shown by Bowcock and Burkhardt [37], the highest multipole fitted in any analysis always tends to accumulate the systematic errors stemming from truncation and is essentially guaranteed to be the most uncertain. Thus, when focusing on multipoles up to $L = 2$ we must vary up to $L = 3$ and fix the multipoles for $4 \leq L \leq 8$ to their (real) Born values. (Details of the Born amplitudes are given in Appendix D.)

To search for a global minimum while allowing for the presence of local minima, we use a Monte Carlo sampling of the multipole parameter space. Values for the real and imaginary parts of the $0 \leq L \leq 3$ multipoles are chosen randomly and their χ^2 comparison to the data of Table III, scaled by the fitted constants in Table IV and Fig. 5, are calculated. Whenever the resulting χ^2 is within 10^4 of the current best, a gradient minimization is carried out. We have repeated this procedure for a wide range of Monte Carlo samples, up to 10^7 per energy, and have found a band of solutions with tightly clustered χ^2 that cannot be distinguished by the existing data. In Figs. 6 and 7 we plot the real and imaginary parts of 300 multipole solutions for which the gradient search has converged to a minimum. The χ^2/point of each solution within these bands is always within 0.2 of the best, and is even more tightly clustered at low energies.

The best and largest values of the χ^2/point for these bands are listed in Table V. (The corresponding multipole solutions are shown as the solid black and blue dashed curves in Figs. 6 and 7, respectively.) The fact that most of the χ^2/point values are substantially less than one is a sign that fitting multipoles up to $L = 3$ provides more freedom than the present collection of data warrant, even though the desired physics demands it.

As a minimum, the bands in Figs. 6 and 7 reflect a relatively shallow valley in the χ^2 space. In an effort to understand if this valley is smooth, indicating a simple broad minimum, or is pitted with many local minima, we have tracked solutions across χ^2. This can be done by forming a hybrid amplitude $A_h(x)$ from two solutions A_1 and A_2:

$$A_h(x) = A_1 \times \left(1 - \frac{x}{100}\right) + A_2 \times \left(\frac{x}{100}\right), \quad x \in [0, 100]. \tag{59}$$

Here x is an effective distance in amplitude-space. For $x = 0$, A_h is just A_1 while for $x = 100$,

TABLE V: Best and largest values of the χ^2/point for the solutions in the bands plotted in Figs. 6 and 7.

E_γ / W (MeV)	Best χ^2/point	Largest χ^2/point
1027 / 1676	0.49	0.54
1122 / 1728	0.59	0.62
1222 / 1781	0.52	0.62
1321 / 1833	0.74	0.92
1421 / 1883	0.97	1.15

A_h becomes A_2. At each value of x between 0 and 100 the hybrid set of multipoles is used to predict observables and the χ^2 relative to the data is calculated. If the valley between A_1 and A_2 were smooth and featureless the resulting χ^2 map would be similarly featureless. We have carried out this exercise between many pairs of solutions and always found pronounced peaks in χ^2 between any pair of A_1 and A_2. As an example, the χ^2/point that results from forming a hybrid amplitude out of the best and largest (worst) solutions of Figs. 6 and 7 is shown in Fig. 8 for two of the energy bins of Table V. (Similar results are obtained at other energies.) At $E_\gamma = 1122$ MeV ($W = 1728$ MeV), in the bottom panel of Fig. 8, the peak in χ^2 between the two is huge. At $E_\gamma = 1421$ MeV ($W = 1883$ MeV) the intermediate peak is still present, though not so tall, probably due to the presence of another local minimum that is nearby but off the direct trajectory between the two solutions.

Evidently the bands in Figs. 6 and 7 are created by clusters of local minima in χ^2 which, for the present collection of data, are completely degenerate and experimentally indistinguishable. The 8 observables in Table III do not yet satisfy the Chiang and Tabakin (CT) criteria as a minimal set that would determine the photoproduction amplitude free of ambiguities [1]. Nonetheless, from studies with mock data we have found that the presence of multiple local minima is essentially universal, even when the CT criteria are satisfied. But, as more observables are added with increasing statistical accuracy the degeneracy is broken and a global minimum emerges. The difficulty then becomes finding it among the pitted landscape in χ^2. Studies of this problem are ongoing and will be discussed elsewhere.

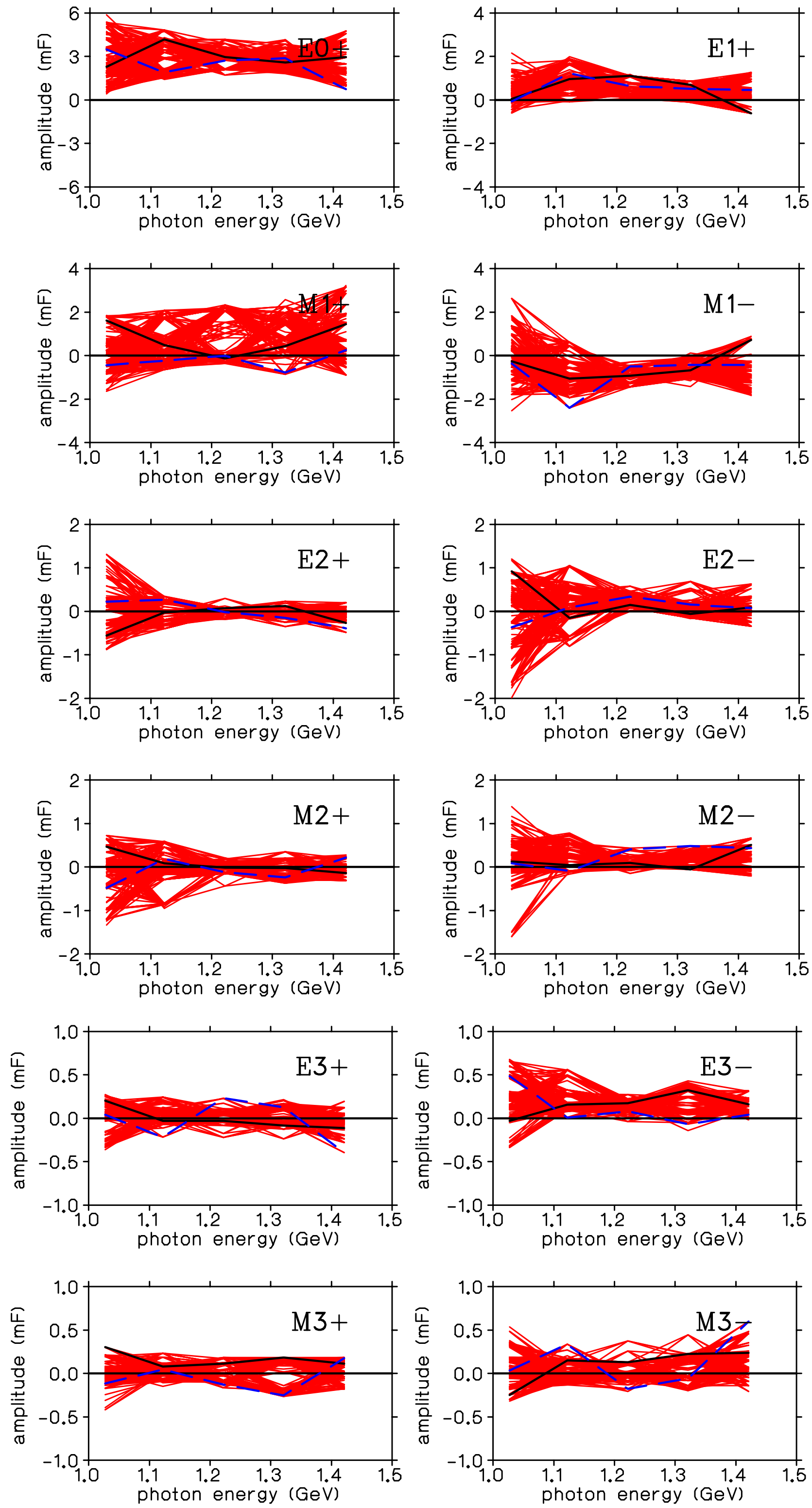

FIG. 6: (Color online) Real parts of multipoles for $L = 0$ to 3, fitted to the data of Table III with the phase of the E_{0+} fixed to 0. The bands show variations in the χ^2/point of less than 0.2, as in Table V. Solutions with the best and largest χ^2, corresponding to the columns of Table V, are shown as solid (black) and long-dashed (blue) curves, respectively.

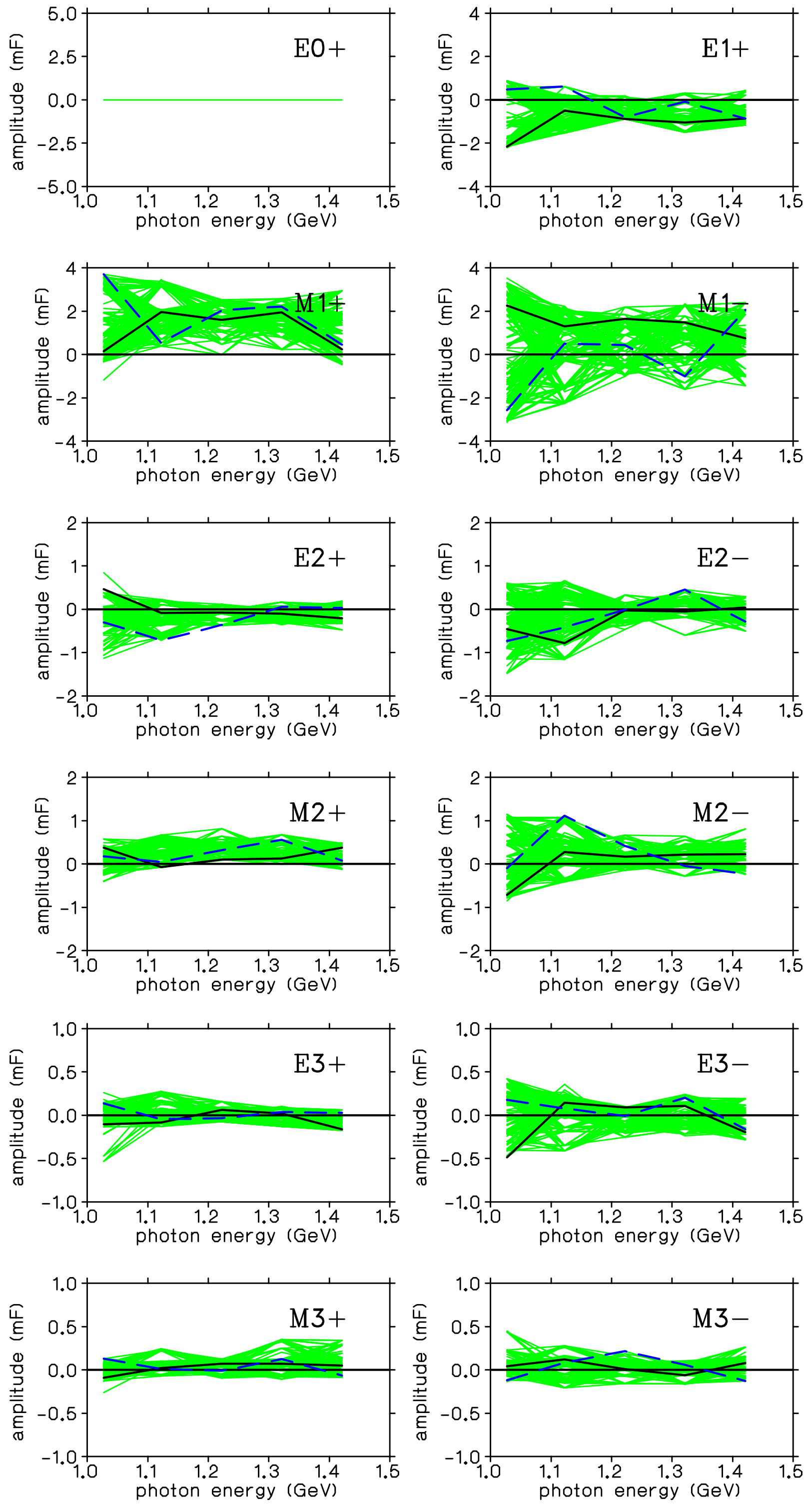

FIG. 7: (Color online) Imaginary parts of multipoles for $L = 0$ to 3, fitted to the data of Table III with the phase of the E_{0+} fixed to 0. The bands show variations in the χ^2/point of less than 0.2, as in Table V. Curves are as in Fig. 6.

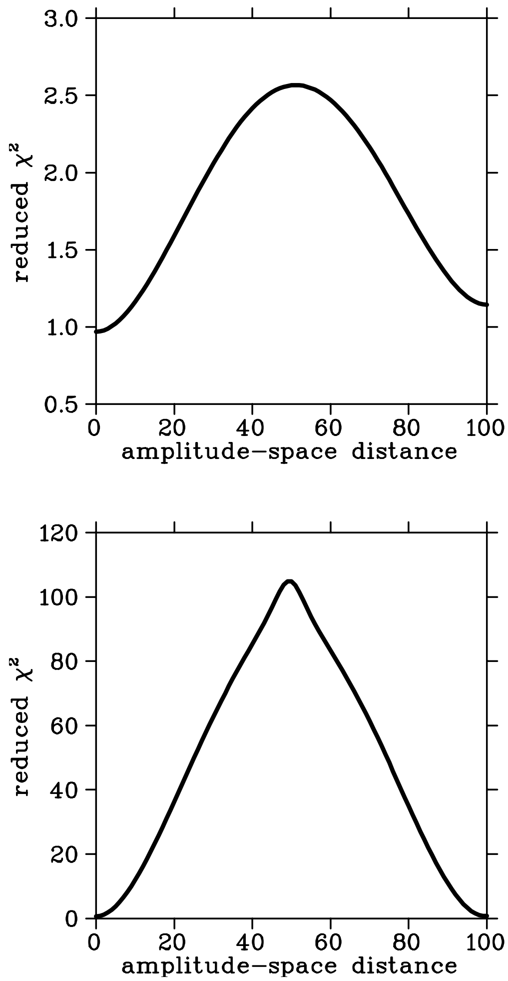

FIG. 8: The χ^2/point calculated by comparing the data of Table III to predictions as a hybrid amplitude [Eq. (59)] is tracked between the solutions with the best and largest χ^2 in Table V (solid black and dashed blue curves in Figs 6 and 7, respectively). Results are shown for E_γ (W) energies of 1122 (1728) MeV in the bottom panel and 1421 (1883) MeV in the top.

D. Constraining the arbitrary phase

In determining an amplitude there is one overall phase that can never be constrained, and so in fitting the solutions of Figs. 6 and 7 we have chosen to fix the phase of the E_{0+} multipole to zero (which sets its imaginary part to zero). The consequence of not fixing a phase is illustrated in Fig. 9, where we plot as an example the S and P wave multipoles from fits with an unconstrained phase angle. Again, the solutions within these bands have values for the χ^2/point that are always within 0.2 of the best. While these bands appear to be substantially broader, they are in fact just the bands of Figs. 6 and 7, expanded by

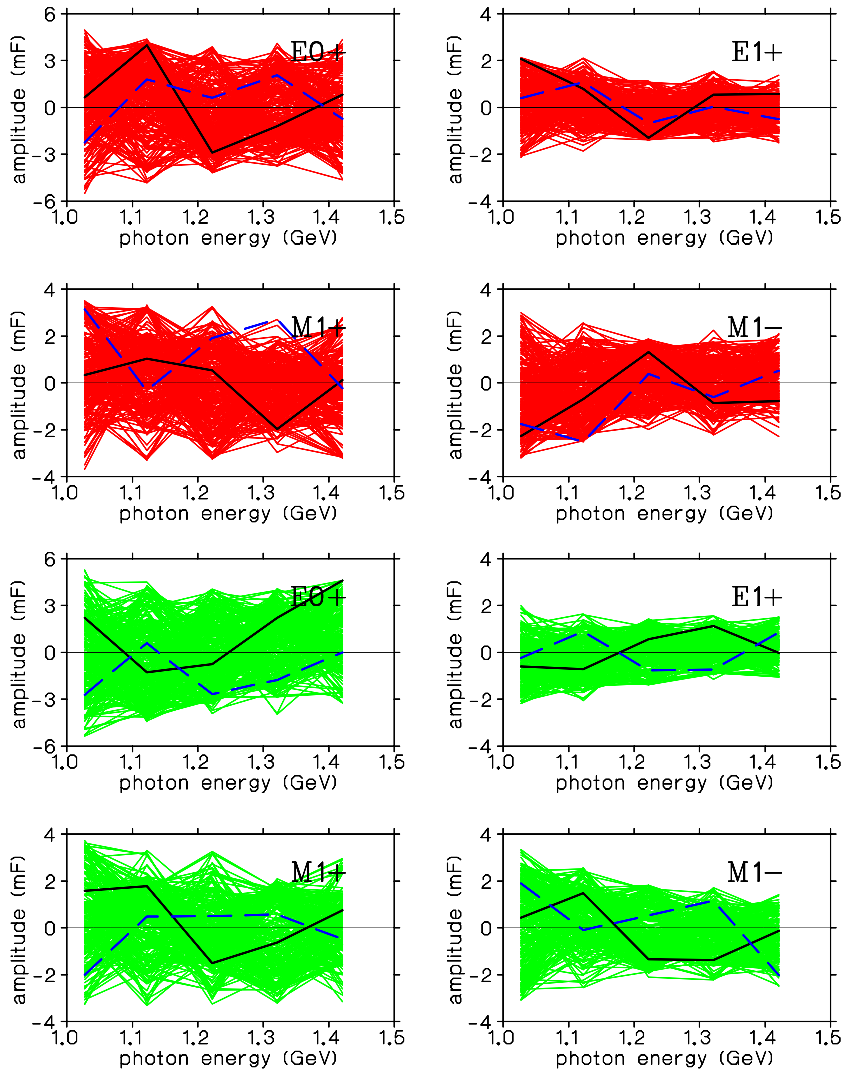

FIG. 9: (Color online) Real (top four panels in red) and imaginary (bottom four panels in green) of the S and P wave multipoles, fitted to the data of Table III without any phase constraints. The bands show variations in the χ^2/point of less than 0.2.

rotating with a random phase angle. The behavior of the $L = 2$ (D) and $L = 3$ (F) waves show a similar broadening.

In practice, the utility of determining a set of multipoles is not diminished by fixing one phase. Ultimately, such experimentally determined multipoles will be compared to model predictions. For this, one only has to rotate the model phase to the same reference point, e.g., a real E_{0+} in the analysis of Figs. 6 and 7. (The result of such an exercise is shown in Figs. 12 and 13.)

The choice of which multipole phase to fix at zero is somewhat arbitrary. From studies with mock data, generated from a known amplitude and gaussian smeared to mimic experiment, we have found that it is sufficient to fix the phase of any one of the larger multipoles ($L = 0, 1$) when the data to be fit have modest statistically accuracy. Ultimately, if the data precision is very high, just fixing the higher L multipoles at their real Born values is enough to recover the amplitude.

E. Constraints from observables – present and future prospects

Predictions of the fitted multipole solutions are compared to the data of Table III in Figs. 10 and 11 for two beam energies, 1122 and 1421 MeV. The best and worst solutions from the bands of Figs. 6 and 7, in terms of the χ^2/point values of Table V, are shown as the solid (black) and dashed (blue) curves, respectively. The behavior at other energies is very similar. Based on such comparisons with existing published data, the multipole solutions within the bands of Figs. 6 and 7 are completely indistinguishable. Clearly, despite the presence of 8 polarization observables, the multipoles are still very poorly constrained. For many of the higher multipoles not even the sign is known.

In Figs. 12 and 13 we compare the S, P and D wave multipoles from existing PWA results (BoGa [27], MAID [22], SAID [25] and JSLT [28]) with the bands of Figs. 6 and 7, respectively. Here we have rotated all multipoles to our common reference point of a real E_{0+}. (Each set of multipoles has been multiplied by $\exp(-i\delta)$, where δ is the phase of the E_{0+} multipole of the PWA set.) For the most part, these PWA lie within our experimental solution bands. However, there are a few exceptions at the higher energies, in particular the M_{2-} multipole from Kaon-MAID (black dashed curve in Fig. 13) and the E_{2-} and M_{2-} multipoles from JSLT (blue solid curves in Fig. 12). The upper end of our analysis range is near a potentially new $N^*(\sim 1900)$. The Kaon-MAID [24] and JSLT groups [28] have associated this feature with the D_{13} partial wave, which should resonate in either the E_{2-} or M_{2-} multipoles. However, our model-independent analysis excludes such conclusions, since their solutions lie outside the experimental bands in these partial waves. On the other hand, the BoGa analysis [38] has recently modeled the $N^*(\sim 1900)$ as a P_{13} resonance, which should manifest itself in either the E_{1+} or M_{1+} multipoles. The BoGa solution is consistently within the experimental solution bands of Figs. 12 and 13. (It is also the only PWA analysis that included the CLAS-g1c and GRAAL data sets in fits of their model parameters.) We

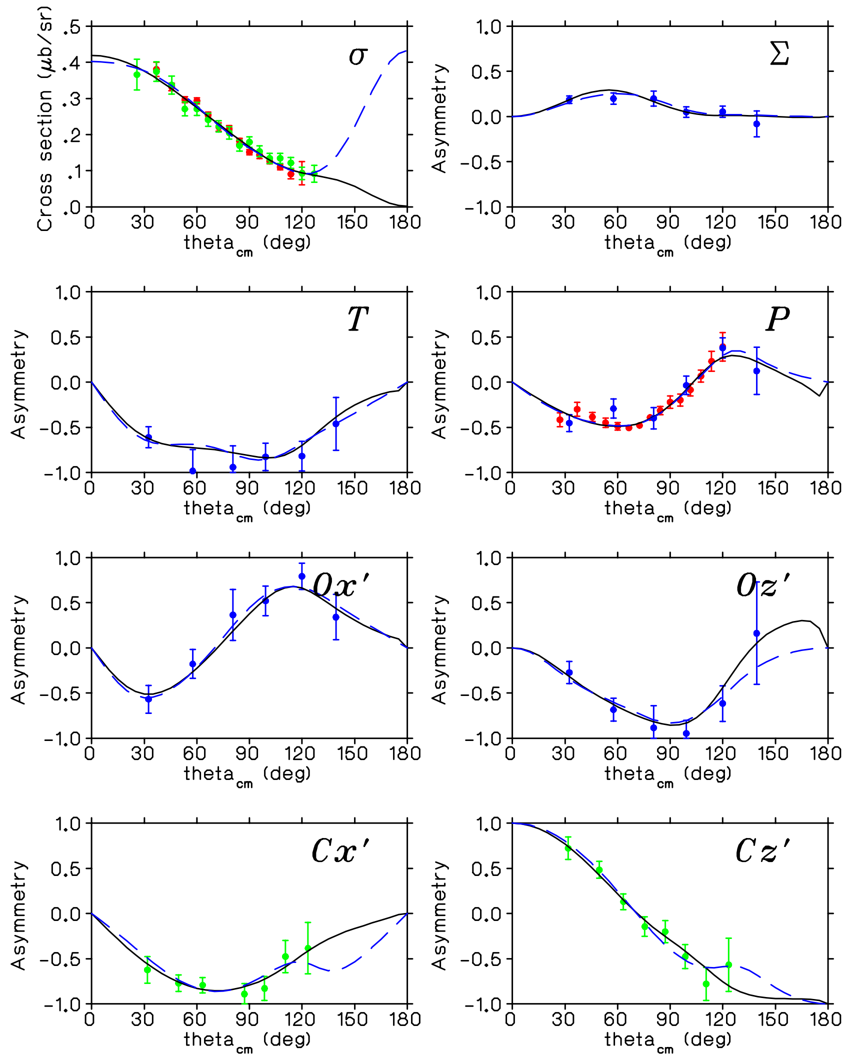

FIG. 10: (Color online) Predictions at $E_\gamma = 1122$ MeV ($W = 1728$ MeV) compared to the data of Table III for the multipole solutions of Figs. 6 and 7 having the minimum (solid black curves) and largest (long-dashed blue curves) χ^2/point (Table V). Data points are from CLAS-g11a [33] shown in red, CLAS-g1c [19, 34] shown in green, and GRAAL [4, 5] shown in blue.

can conclude that their assignment is consistent with the experimental solution bands, but cannot yet confirm it due to the significant width of these bands.

We have investigated a number of possible ways in which additional data may lead to narrower multipole bands and improved amplitude definition. For the most part, existing data does not reach to extreme angles (near 0° and 180°), which in general tend to be more sensitive to interfering multipoles of opposite parity. In fact, the best and worst solutions at $E_\gamma = 1122$ MeV ($W = 1728$ MeV) exhibit a dramatic difference in the predicted unpolarized

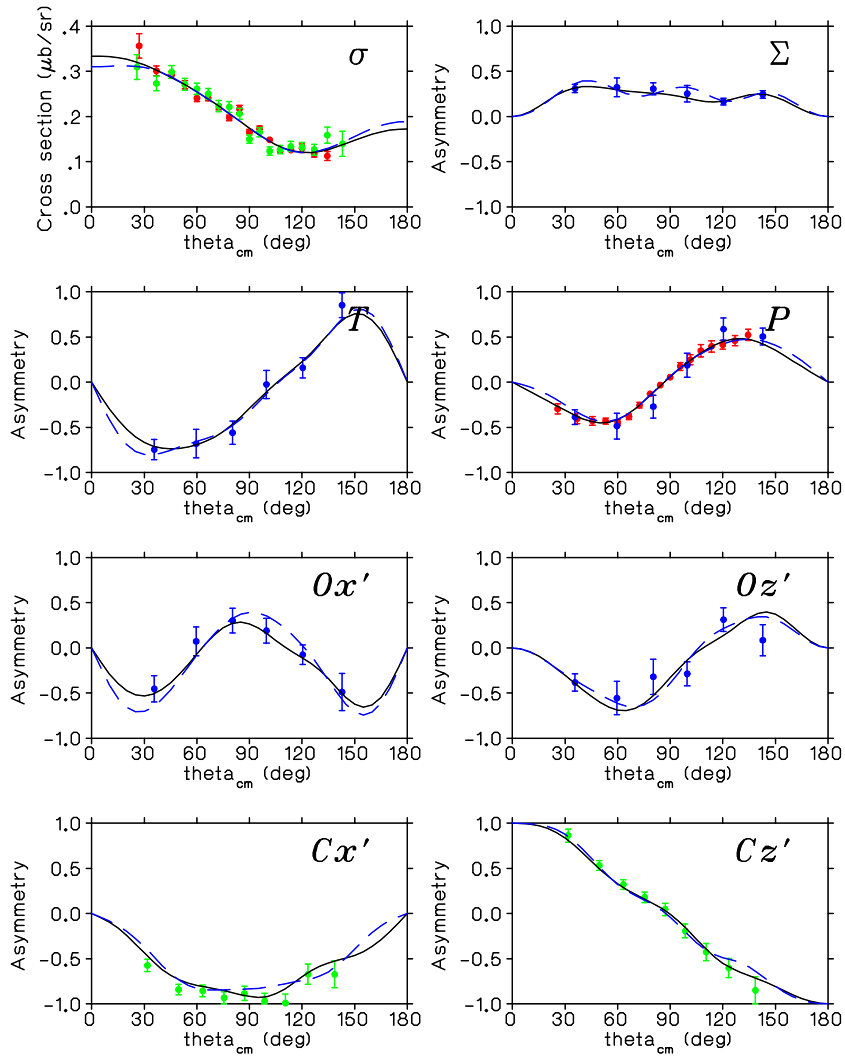

FIG. 11: (Color online) Predictions at $E_\gamma = 1421$ MeV ($W = 1883$ MeV) compared to the data of Table III for the multipole solutions of Figs. 6 and 7 having the minimum (solid black curves) and largest (long-dashed blue curves) χ^2/point (Table V). Data points are plotted as in Fig. 10.

cross section at 180° – compare the solid (black) and dashed (blue) curves in Fig. 10. (The extreme angles of the asymmetries are constrained by symmetry to either 0 or ±1, and so contain little additional information.) As a test, we have created mock cross section data at 0° and 180°, centered on the best solutions of Table V with a statistical error of $\pm 0.03\mu$b/sr. When the fits are repeated with these mock points added to the CLAS and GRAAL data sets, variations such as seen in Fig. 10 disappear, but few of the resulting bands of multipole solutions are improved. While the M_{1+}, M_{1-} and E_{2-} are slightly narrowed at low energies, generally, there is little improvement over the trends of Figs. 6 and 7.

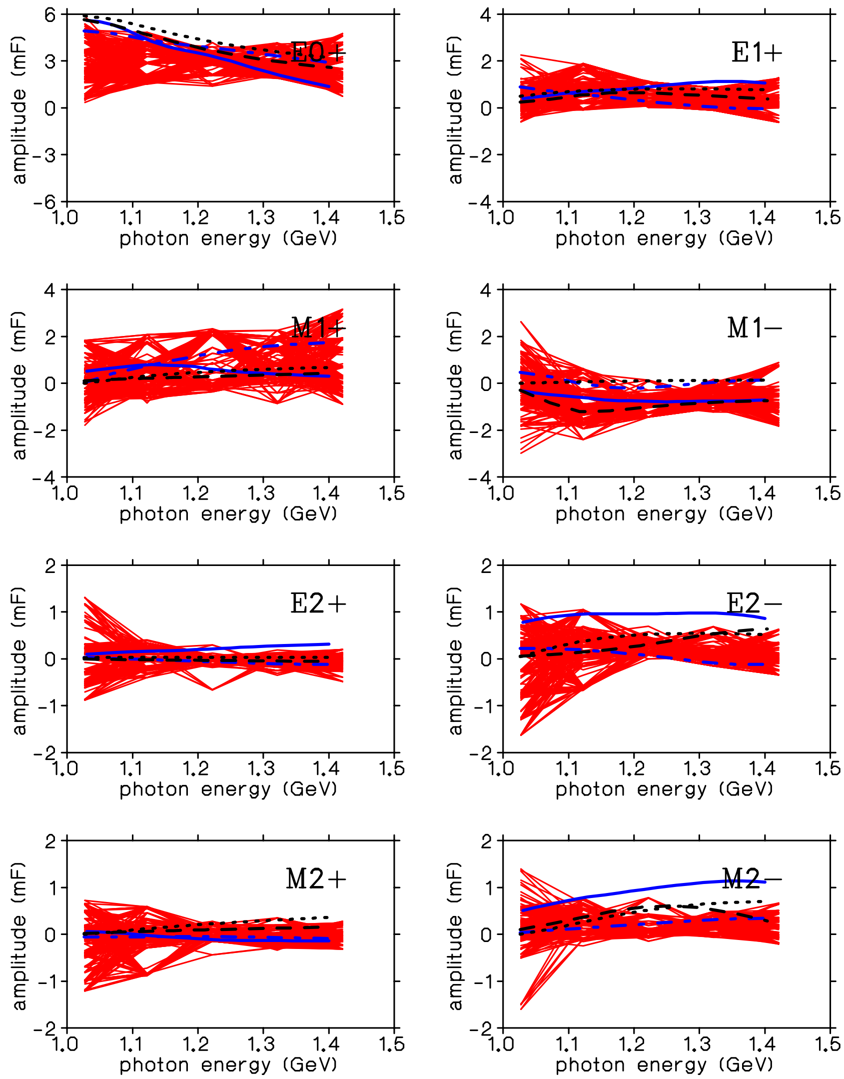

FIG. 12: (Color online) The solution bands of Fig. 6, compared to the real parts of PWA multipoles of BoGa [27] (blue dashed-dot), Kaon-MAID [22] (black dashed), SAID [25] (black dotted) and JSLT [28] (blue solid).

The data of Table III span a significant range in statistical precision. From preliminary analyses of data from an ongoing generation of new CLAS experiments we can anticipate result on the Σ, T, $O_{x'}$ and $O_{z'}$ asymmetries that will have roughly an order of magnitude improvement over the GRAAL data set. To simulate the effect of such an improvement, we have arbitrarily reduced the statistical errors on the GRAAL Σ, T, $O_{x'}$ and $O_{z'}$ asymmetries by a factor of 3 and repeated the fits. Apart from an increase in χ^2, due to undulations in the angular distributions that are now artificially beyond the level of statistical fluctuations, there are no significant changes in any of the multipole bands of Figs. 6 and 7.

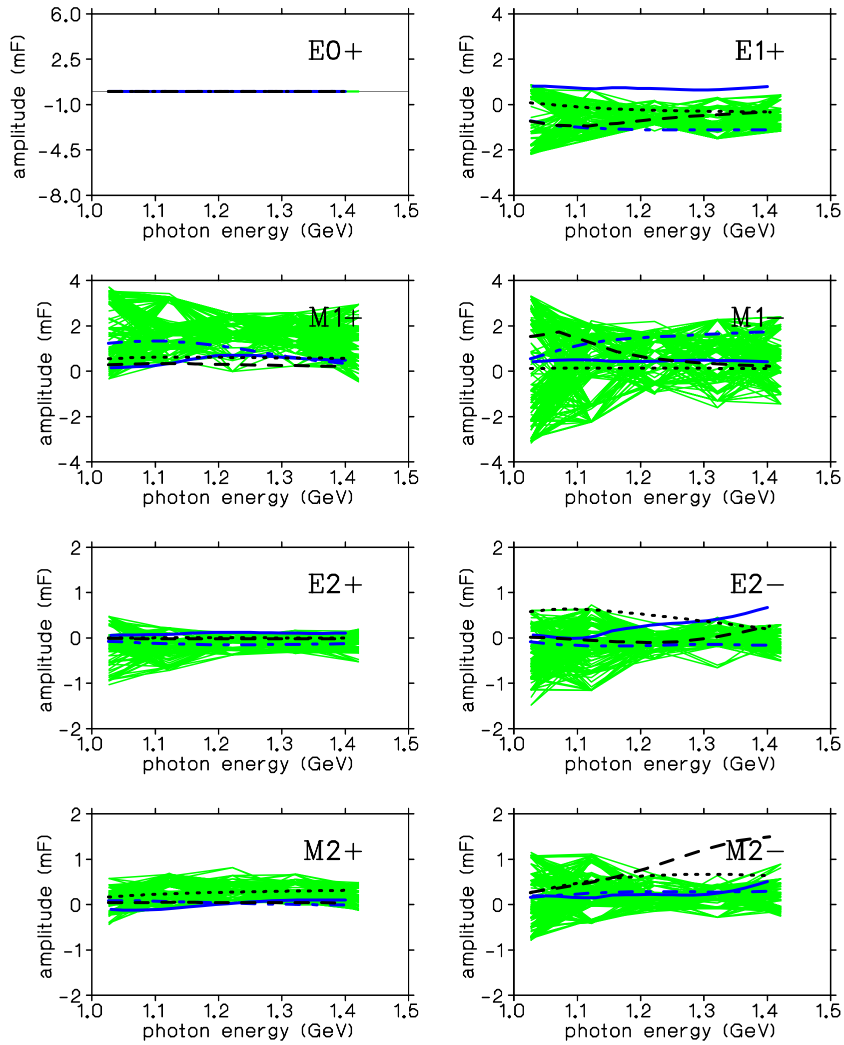

FIG. 13: (Color online) The solution bands of Fig. 7, compared to the imaginary parts of PWA multipoles of BoGa [27] (blue dashed-dot), Kaon-MAID [22] (black dashed), SAID [25] (black dotted) and JSLT [28] (blue solid).

Ongoing analyses of new experiments are expected to yield data on all 16 observables. We can get some inkling of the effect of such an expanded data set by examining the impact that the GRAAL measurements of (Σ, T, $O_{x'}$, $O_{z'}$) have made so far. In Fig. 14 we show the S and P wave multipoles obtained if the GRAAL data are removed from the fitting procedure. Comparing these results to Figs. 6 and 7, it is clear that the M_{1+} band has dramatically narrowed with the inclusion of the GRAAL polarization results. Lesser but still significant gains in definition occur in most of the multipoles. The range of values for the χ^2/point within these bands are similar to those of Table V. In Fig. 15 we show the

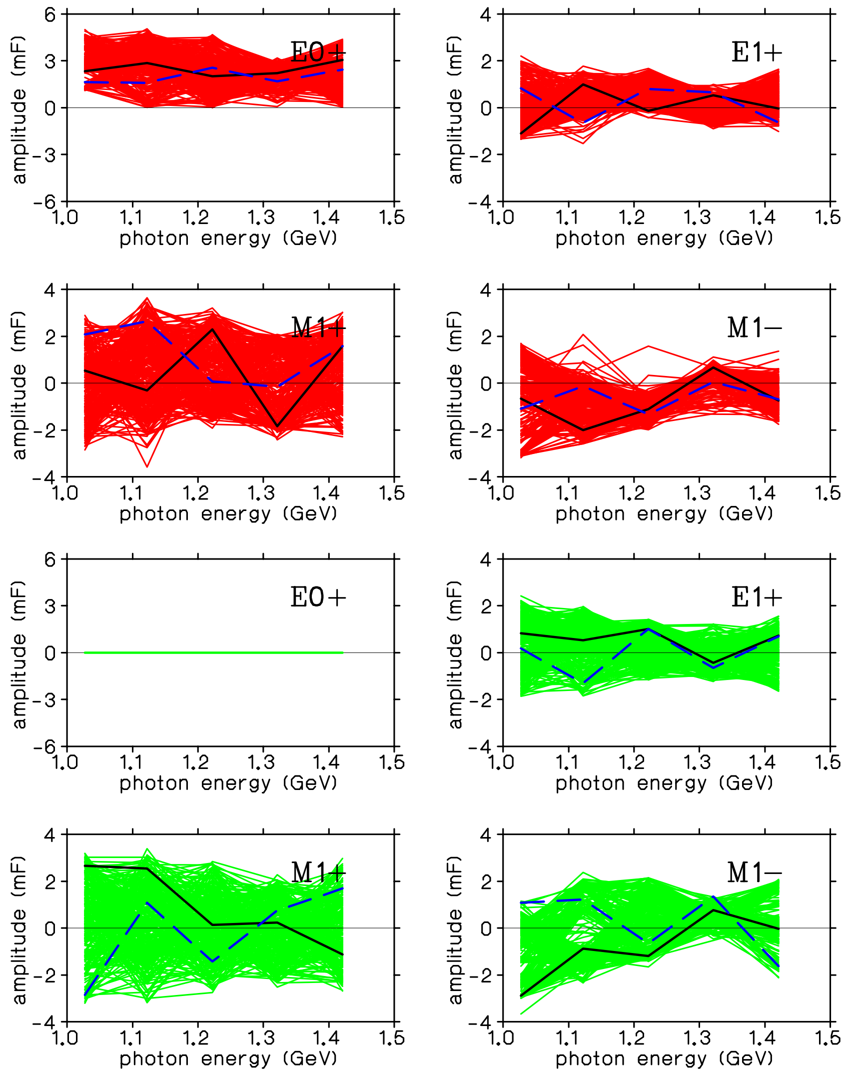

FIG. 14: (Color online) Real (top 4 panels in red) and imaginary (bottom 4 panels in green) of the S and P wave multipoles, fitted to the CLAS data of Table III (excluding the GRAAL measurements). Solutions with the best (1.07) and largest (1.18) χ^2 are shown as solid (black) and long-dashed (blue) curves, respectively.

predictions of the band at 1421 MeV beam energy (W = 1883 MeV), as represented by the solutions with the minimum χ^2/point = 1.07 and the maximum χ^2/point = 1.18. Not surprisingly, predictions for the observables where data have been removed from the fit are now wildly varied.

There are several conclusions that can be drawn from this analysis, along with reasons for genuine hope. When the χ^2/point is near or even better than 1, solutions differing in the χ^2/point by something like 0.2 are not experimentally distinguishable. The existence

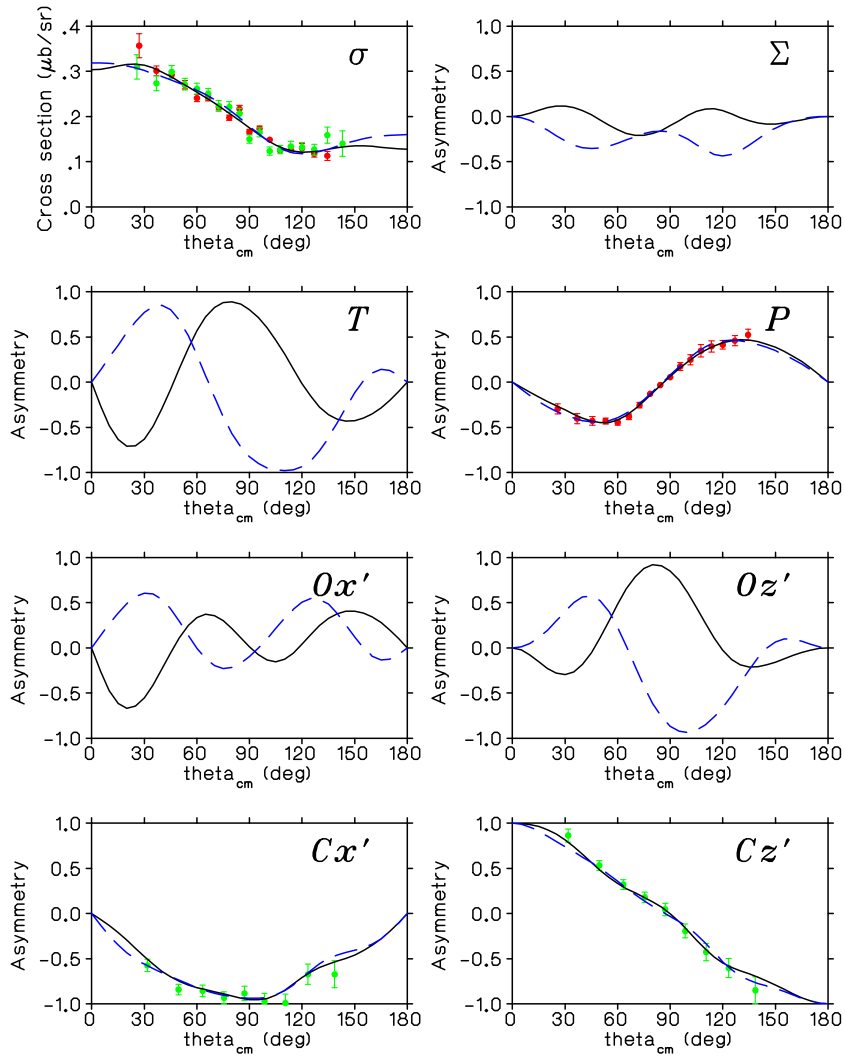

FIG. 15: (Color online) Predictions at $E_\gamma = 1421$ MeV ($W = 1883$ MeV) from a multipole fit to the CLAS data from CLAS-g11a [33] shown in red and CLAS-g1c [19, 34] shown in green, excluding the GRAAL results. The solid black and long-dashed blue curves show the solutions (Fig. 14) having the minimum (1.07) and largest (1.18) χ^2/point.

of bands of multipole solutions, each with small χ^2/point, indicates a shallow χ^2 surface, pitted with many local minima. Certainly the width of the bands evident in Figs. 6 and 7 precludes using the existing data to *hunt for resonances*. However, comparing Fig. 14 and Figs. 6 and 7, the gains evident from the GRAAL polarization observables are significant, even though the GRAAL errors are substantially larger than most of the CLAS data. CLAS data on all 16 photoproduction observables are now under analysis. The fact that such data have all been accumulated within a single detector is likely to minimize the problems evident in Fig. 4. Furthermore, with a large number of different observables will come a large number of the Fierz identities, which can be used to constrain the systematic scale uncertainties.

IX. SUMMARY

It is anticipated that data will soon be available on all 16 pseudoscalar meson photoproduction observables from a new generation of ongoing experiments, certainly for $K\Lambda$ final states and possibly for πN channels as well. This will significantly reduce the model dependence in the study of excited baryon structure by providing a total amplitude that is experimentally determined to within a phase. Such an experimental amplitude can be utilized at two levels, first as a test to validate total amplitudes associated with different models and second as a starting point that can be analytically continued into the complex plane to search for poles. Here we have laid the ground work for this by assembling a consistent set of equations needed for amplitude reduction from experiment and have demonstrated the first stage of interaction with theoretical models.

In summary, we have used direct numerical evaluations, Eqs. (32)-(35), to verify the most general analytic form of the cross section, dependent on the three polarization vectors of the beam, target and recoil baryon, including all single, double and triple-polarization terms involving the 16 possible spin-dependent observables [Eq. (37)]. (Copies of the associated computer code are available upon request [39].) We have explicitly listed the experimental measurements needed to construct each observable in pseudoscalar meson photoproduction (Appendix B) and provided a consistent set of equations relating these quantities to the CGLN amplitudes [Eq. (53)], and from these to electromagnetic multipoles. We have used our independent method of numerical evaluation to resolve sign differences that exist in the literature. We have found the BoGa PWA to be completely self-consistent and in agreement with the present work, once one accounts for a difference in the definition of the E asymmetry. We find the MAID PWA to be completely self-consistent, but with a different choice of signs in the definitions of the six H, $L_{x'}$, $C_{x'}$, $C_{z'}$, $O_{x'}$ and $O_{z'}$ asymmetries, which is the negative of what is commonly assumed by experimental groups. Comparing to the SAID PWA, we find sign differences when compared to our work in the same six observables. The papers documenting the SAID PWA do not include analytic expressions for the general cross section or explicit definitions of the observables, referring rather to BDS [7] for the latter. Although the notation in the BDS paper is rather condensed, their definitions of observables appear to agree with ours, which forces us to conclude that the SAID choice of signs is not internally self-consistent. We have numerically checked the signs in the 37 Fierz identities that interrelate the 16 spin-dependent observables and have provided a consistent set (Appendix C).

We have used the assembled machinery to carry out a multipole analysis of the $\gamma p \to K^+\Lambda$ reaction, free of model assumptions, and examined the impact of recently published measurements on 8 different observables. We have used a combined Monte Carlo sampling of the amplitude space, with gradient minimization, and have found a shallow χ^2 valley pitted with a very large number of local minima that results in broad bands of multipole solutions, which are experimentally indistinguishable (Figs. 6 and 7). Comparing to models that have recently reported a new $N^*(\sim 1900)$, we can exclude PWA that include a new D_{13} since their amplitudes lie outside the model-independent solution bands in the associated multipoles. (These PWA were carried out before most of the data used in our analysis were available.) Recent BoGa analyses have modeled the $N^*(\sim 1900)$ as a P_{13} resonance. While their solution lies with our experimental multipole bands, we cannot yet validate it due to the significant width of the bands.

From our studies, as well as simulations with mock data, we have seen that clusters of local minima in χ^2 are always present. With the current collection of results on 8 observables, these minima are completely degenerate and experimentally indistinguishable. In studies with mock data we have seen this degeneracy broken with high precision data on large numbers of observables. As in the present analysis, a greater number of different observables tend to be more effective in creating a global minimum than higher precision. We conclude that, while a general solution to the problem of determining an amplitude free of ambiguities may require 8 observables, as has been discussed by CT [1], such requirements assume data of arbitrarily high precision. Experiments with realistically achievable uncertainties will require a significantly larger number.

Acknowledgments

This work was supported by the U.S. Department of Energy, Office of Nuclear Physics Division, under Contract No. DE-AC05-060R23177 under which Jefferson Science Associates operates Jefferson Laboratory, and also by the U.S. Department of Energy, Office of Nuclear Physics Division, under Contract No. DE-AC02-06CH11357 and Contract No. DE-FG02-97ER41025.

Appendix A: General expression for the differential cross section with fixed polarizations

We summarize here the derivation of an analytic expression for the differential cross section in pseudoscalar meson photoproduction with general values of the beam, target and recoil polarization. Following the formalism of the spin density matrices described by FTS [11], one can write the general cross section [Eq. (35)] as,

$$d\sigma_{\mathrm{B,T,R}}(\vec{P}^{\gamma}, \vec{P}^{T}, \vec{P}^{R}) \;=\; \rho_0(\rho^R)_{kn}(F_\mu)_{nm}(\rho^T)_{ml}(F^\dagger_\lambda)_{lk}(\rho^\gamma)_{\mu\lambda}. \tag{A1}$$

(Throughout this appendix the same indices in equations imply taking summation.) Here $\rho_0 = k/q$; $(F_\lambda)_{m_{s_\Lambda} m_{s_N}} = \langle m_{s_\Lambda}|F_{\mathrm{CGLN}}|m_{s_N}\rangle$, in which the spin states of the initial and final baryons are quantized in the z-direction and the (unit) photon polarization vector is taken to be circularly polarized with the helicity λ.

The 2×2 spin density matrix ρ^X for $X = \gamma, T, R$ is given by

$$\rho^\gamma \;=\; \frac{1}{2}[\mathbf{1} + \vec{\mathcal{P}}^\gamma \cdot \vec{\sigma}], \tag{A2}$$

$$\rho^T \;=\; \frac{1}{2}[\mathbf{1} + \vec{P}^T \cdot \vec{\sigma}], \tag{A3}$$

$$\rho^R \;=\; \frac{1}{2}[\mathbf{1} + \vec{P}^R \cdot \vec{\sigma}], \tag{A4}$$

where $\vec{\sigma}$ is the Pauli spin vector, as in Eq. (24), and $\vec{\mathcal{P}}^\gamma$ is the so-called Stokes vector for the photon polarizations [11]. Note that in the x-y-z coordinate (see Fig. 2), $\vec{\mathcal{P}}^\gamma = (-P^\gamma_L \cos 2\phi_\gamma, -P^\gamma_L \sin 2\phi_\gamma, P^\gamma_c)$.

Substituting Eqs. (A2)-(A4) into Eq. (A1), we have

$$
\begin{aligned}
d\sigma_{\mathrm{B,T,R}}(\vec{P}^{\gamma},\vec{P}^{T},\vec{P}^{R}) &= \rho_0 \frac{1}{2}(\mathbf{1}+\vec{P}^{R}\cdot\vec{\sigma})_{kn}(F_\mu)_{nm}\frac{1}{2}(\mathbf{1}+\vec{P}^{T}\cdot\vec{\sigma})_{ml}(F^\dagger_\lambda)_{lk}\frac{1}{2}(\mathbf{1}+\vec{\mathcal{P}}^{\gamma}\cdot\vec{\sigma})_{\mu\lambda} \\
&= \frac{\rho_0}{8}(\mathbf{1}+\vec{P}^{R}\cdot\vec{\sigma})_{kn}\Big[(F_\lambda)_{nm}(F^\dagger_\lambda)_{mk}+(F_\mu)_{nm}(F^\dagger_\lambda)_{mk}\vec{\mathcal{P}}^{\gamma}\cdot\vec{\sigma}_{\mu\lambda} \\
&\quad +(F_\lambda)_{nm}\vec{P}^{T}\cdot\vec{\sigma}_{ml}(F^\dagger_\lambda)_{lk}+(F_\mu)_{nm}\vec{P}^{T}\cdot\vec{\sigma}_{ml}(F^\dagger_\lambda)_{lk}\vec{\mathcal{P}}^{\gamma}\cdot\vec{\sigma}_{\mu\lambda}\Big]. \qquad \text{(A5)}
\end{aligned}
$$

Noting that $d\sigma_0 = (\rho_0/4)\mathcal{N}$ where $\mathcal{N} = (F_\lambda)_{nm}(F^\dagger_\lambda)_{mn}$, the above equation can be further expanded as

$$
\begin{aligned}
d\sigma_{\mathrm{B,T,R}}(\vec{P}^{\gamma},\vec{P}^{T},\vec{P}^{R}) &= \frac{d\sigma_0}{2}\Bigg\{1+(\vec{\mathcal{P}}^{\gamma})^{a}\frac{(F_\mu)_{kn}(F^\dagger_\lambda)_{nk}\sigma^a_{\mu\lambda}}{\mathcal{N}}+(\vec{P}^{T})^{a}\frac{(F_\lambda)_{kn}\sigma^a_{nm}(F^\dagger_\lambda)_{mk}}{\mathcal{N}} \\
&\quad +(\vec{P}^{R})^{a'}\frac{\sigma^{a'}_{kn}(F_\lambda)_{nm}(F^\dagger_\lambda)_{mk}}{\mathcal{N}} \\
&\quad +(\vec{P}^{T})^{a}(\vec{\mathcal{P}}^{\gamma})^{b}\frac{(F_\mu)_{km}\sigma^a_{ml}(F^\dagger_\lambda)_{lk}\sigma^b_{\mu\lambda}}{\mathcal{N}}+(\vec{P}^{R})^{a'}(\vec{\mathcal{P}}^{\gamma})^{b}\frac{\sigma^{a'}_{kn}(F_\mu)_{nl}(F^\dagger_\lambda)_{lk}\sigma^b_{\mu\lambda}}{\mathcal{N}} \\
&\quad +(\vec{P}^{R})^{a'}(\vec{P}^{T})^{a}\frac{\sigma^{a'}_{kn}(F_\lambda)_{nm}\sigma^a_{ml}(F^\dagger_\lambda)_{lk}}{\mathcal{N}} \\
&\quad +(\vec{P}^{R})^{a'}(\vec{P}^{T})^{a}(\vec{\mathcal{P}}^{\gamma})^{b}\frac{\sigma^{a'}_{kn}(F_\mu)_{nm}\sigma^a_{ml}(F^\dagger_\lambda)_{lk}\sigma^b_{\mu\lambda}}{\mathcal{N}}\Bigg\} \\
&= \frac{d\sigma_0}{2}\Big\{1+(\vec{\mathcal{P}}^{\gamma})^{a}\boldsymbol{\Sigma}^a+(\vec{P}^{T})^{a}\boldsymbol{T}^a+(\vec{P}^{R})^{a'}\boldsymbol{P}^{a'} \\
&\quad +(\vec{P}^{T})^{a}(\vec{\mathcal{P}}^{\gamma})^{b}C^{\mathrm{BT}}_{ab}+(\vec{P}^{R})^{a'}(\vec{\mathcal{P}}^{\gamma})^{a}C^{\mathrm{BR}}_{ab}+(\vec{P}^{R})^{a'}(\vec{P}^{T})^{a}C^{\mathrm{TR}}_{a'b} \\
&\quad +(\vec{P}^{R})^{a'}(\vec{P}^{T})^{a}(\vec{\mathcal{P}}^{\gamma})^{b}C^{\mathrm{BTR}}_{a'ab}\Big\}. \qquad \text{(A6)}
\end{aligned}
$$

In the last step we have introduced

$$\boldsymbol{\Sigma}^a = \frac{(F_\mu)_{kn}(F^\dagger_\lambda)_{nm}\sigma^a_{\mu\lambda}}{\mathcal{N}}, \qquad \text{(A7)}$$

$$\boldsymbol{T}^a = \frac{(F_\lambda)_{kn}\sigma^a_{nm}(F^\dagger_\lambda)_{mk}}{\mathcal{N}}, \qquad \text{(A8)}$$

$$\boldsymbol{P}^{a'} = \frac{\sigma^{a'}_{kn}(F_\lambda)_{nm}(F^\dagger_\lambda)_{mk}}{\mathcal{N}}, \qquad \text{(A9)}$$

$$C^{\mathrm{BT}}_{ab} = \frac{(F_\mu)_{kn}\sigma^a_{nm}(F^\dagger_\lambda)_{mk}\sigma^b_{\mu\lambda}}{\mathcal{N}}, \qquad \text{(A10)}$$

$$C^{\mathrm{BR}}_{a'b} = \frac{\sigma^{a'}_{kn}(F_\mu)_{nm}(F^\dagger_\lambda)_{mk}\sigma^a_{\mu\lambda}}{\mathcal{N}}, \qquad \text{(A11)}$$

$$C^{\mathrm{TR}}_{a'b} = \frac{\sigma^{a'}_{kn}(F_\lambda)_{nm}\sigma^a_{ml}(F^\dagger_\lambda)_{lk}}{\mathcal{N}}, \qquad \text{(A12)}$$

$$C^{\mathrm{BTR}}_{a'ab} = \frac{\sigma^{a'}_{kn}(F_\mu)_{nm}\sigma^a_{ml}(F^\dagger_\lambda)_{lk}\sigma^b_{\mu\lambda}}{\mathcal{N}}. \qquad \text{(A13)}$$

Also, in Eqs. (A6)-(A13) the inner products $\vec{\mathcal{P}}^\gamma \cdot \vec{\sigma}$ and $\vec{P}^T \cdot \vec{\sigma}$ are expressed with the components in the unprimed x-y-z coordinate, while in the primed x'-y'-z' coordinate for that of recoil baryon $\vec{P}^R \cdot \vec{\sigma}$: $\vec{\mathcal{P}}^\gamma \cdot \vec{\sigma} = (\vec{\mathcal{P}}^\gamma)^a \sigma^a = (\vec{\mathcal{P}}^\gamma)^x \sigma^x + (\vec{\mathcal{P}}^\gamma)^y \sigma^y + (\vec{\mathcal{P}}^\gamma)^z \sigma^z$ and $\vec{P}^T \cdot \vec{\sigma} = (\vec{P}^T)^a \sigma^a = (\vec{P}^T)^x \sigma^x + (\vec{P}^T)^y \sigma^y + (\vec{P}^T)^z \sigma^z$ whereas $\vec{P}^R \cdot \vec{\sigma} = (\vec{P}^R)^{a'} \sigma^{a'} = (\vec{P}^R)^{x'} \sigma^{x'} + (\vec{P}^R)^{y'} \sigma^{y'} + (\vec{P}^R)^{z'} \sigma^{z'}$, where $(\sigma^{x'}, \sigma^{y'}, \sigma^{z'})$ is related to the Pauli matrices (24) through Eqs. (38) and (39). (If the unprimed x-y-z coordinates are used also to express $\vec{P}^R \cdot \vec{\sigma}$, then one obtain unprimed observables.)

We note that $\boldsymbol{\Sigma}^a$, $\boldsymbol{T}^a$, $\boldsymbol{P}^a$, C^{BT}_{ab}, $C^{\mathrm{BR}}_{a'b}$, and $C^{\mathrm{TR}}_{a'b}$ are exactly the same as those defined in Ref. [11]. The $C^{\mathrm{BTR}}_{a'ab}$ term was not included in Ref. [11], since they did not discuss the triple polarization case. Each component in Eqs. (A7)-(A13) can be related with 16 observables defined in Tables VI-IX of Appendix B:

$$\boldsymbol{\Sigma}^{x_B} = \Sigma,\ \boldsymbol{T}^{y_T} = T,\ \boldsymbol{P}^{y'_R} = P, \tag{A14}$$

$$C^{\mathrm{BT}}_{z_T z_B} = -E,\ C^{\mathrm{BT}}_{z_T y_B} = -G,\ C^{\mathrm{BT}}_{x_T z_B} = F,\ C^{\mathrm{BT}}_{x_T y_B} = -H,\ C^{\mathrm{BT}}_{y_T x_B} = P, \tag{A15}$$

$$C^{\mathrm{BR}}_{z'_R z_B} = C_{z'},\ C^{\mathrm{BR}}_{z'_R y_B} = -O_{z'},\ C^{\mathrm{BR}}_{x'_R z_B} = C_{x'},\ C^{\mathrm{BR}}_{x'_R y_B} = -O_{x'},\ C^{\mathrm{BR}}_{y'_R x_B} = T, \tag{A16}$$

$$C^{\mathrm{TR}}_{z'_R z_T} = L_{z'},\ C^{\mathrm{TR}}_{z'_R x_T} = T_{z'},\ C^{\mathrm{TR}}_{x'_R z_T} = L_{x'},\ C^{\mathrm{TR}}_{x'_R x_T} = T_{x'}, C^{\mathrm{TR}}_{y'_R y_T} = T, \tag{A17}$$

$$\begin{aligned}
&C^{\mathrm{BTR}}_{y'_R x_T y_B} = -E, && C^{\mathrm{BTR}}_{y'_R x_T z_B} = G, && C^{\mathrm{BTR}}_{y'_R z_T y_B} = -F, && C^{\mathrm{BTR}}_{y'_R z_T z_B} = -H,\\
&C^{\mathrm{BTR}}_{x'_R y_T y_B} = -C_{z'}, && C^{\mathrm{BTR}}_{x'_R y_T z_B} = -O_{z'}, && C^{\mathrm{BTR}}_{z'_R y_T y_B} = C_{x'}, && C^{\mathrm{BTR}}_{z'_R y_T z_B} = O_{x'},\\
&C^{\mathrm{BTR}}_{x'_R x_T x_B} = L_{z'}, && C^{\mathrm{BTR}}_{x'_R z_T x_B} = -T_{z'}, && C^{\mathrm{BTR}}_{z'_R x_T x_B} = -L_{x'}, && C^{\mathrm{BTR}}_{z'_R z_T x_B} = T_{x'},\\
&C^{\mathrm{BTR}}_{y'_R y_T x_B} = 1.
\end{aligned} \tag{A18}$$

Here all other components not explicitly shown are identically zero; these result from symmetry constraints.

Finally, we also note that the spin density matrices (A2)-(A4) can be expressed as

$$\rho^\gamma = \sum_{\hat{P} = \hat{P}_1^\gamma, \hat{P}_2^\gamma} \mathfrak{p}^\gamma_{\hat{P}} \frac{1}{2}[\mathbf{1} + \hat{\mathcal{P}}_{\hat{P}} \cdot \sigma], \tag{A19}$$

$$\rho^T = \sum_{\hat{Q} = \pm \hat{P}^T} \mathfrak{p}^T_{\hat{Q}} \frac{1}{2}[\mathbf{1} + \hat{Q} \cdot \sigma], \tag{A20}$$

$$\rho^R = \sum_{\hat{R} = \pm \hat{P}^R} \mathfrak{p}^R_{\hat{R}} \frac{1}{2}[\mathbf{1} + \hat{R} \cdot \sigma]. \tag{A21}$$

Here $\mathfrak{p}^X_{\hat{P}}$ is the probability observing particle X polarized in the $\hat{P}$ direction; $\hat{\mathcal{P}}_{\hat{P}}$ is the Stokes vector specified by the unit photon polarization vector $\hat{P}$; $\hat{P}_2^\gamma$ is a unit photon polarization vector perpendicular to $\hat{P}_1^\gamma \equiv \hat{P}^\gamma$ for linearly polarized photons, while $\hat{P}_1^\gamma$ and $\hat{P}_2^\gamma$ express two different helicity states for circularly polarized photons. The non-unit polarization vectors can be expressed with the unit polarization vectors as $\vec{P}^\gamma = (\mathfrak{p}^\gamma_{\hat{P}_1^\gamma} - \mathfrak{p}^\gamma_{\hat{P}_2^\gamma})\hat{P}^\gamma$, $\vec{P}^T = (\mathfrak{p}^T_{+\hat{P}^T} - \mathfrak{p}^T_{-\hat{P}^T})\hat{P}^T$, and $\vec{P}^R = (\mathfrak{p}^R_{+\hat{P}^R} - \mathfrak{p}^R_{-\hat{P}^R})\hat{P}^R$. Substituting Eqs. (A19)-(A21) into Eq. (A1), one obtain the relation between the general cross sections with unit and non-unit polarization vectors [Eq. (35)].

Appendix B: Constructing Observables from Measurements

We tabulate here the pairs of measurements needed to construct each of the 16 transverse photoproduction observables in terms of the polarization orientation angles of Fig. 2. The photon beam is characterized either by its helicity, h_γ for circular polarization, or by ϕ_γ^L for linear polarization. Assuming 100% polarizations, each observable $\hat{A} = A d\sigma_0$ is determined by a pair of measurements, each denoted as $\sigma(B, T, R)$; "*unp*" indicates the need to average over the initial spin states of the target and/or beam, and to sum over the final spin states of the recoil baryon. For observables involving only beam and/or target polarizations, $d\sigma_0 = (1/2)(\sigma_1 + \sigma_2)$ and $\hat{A} = (1/2)(\sigma_1 - \sigma_2)$. For observables involving the final state recoil polarization, $d\sigma_0 = (\sigma_1 + \sigma_2)$ and $\hat{A} = (\sigma_1 - \sigma_2)$.

TABLE VI: The cross section and the observables with only one polarization in their leading term of Eq. (37); $d\sigma_0 = \beta(\sigma_1 + \sigma_2)$ and $\hat{A} = \beta(\sigma_1 - \sigma_2)$, where $\beta = 1$ ($\beta = 1/2$) if recoil polarization is (is not) observed.

$d\sigma_0$, Σ, T, P		Beam		Target		Recoil	
Observable	$(\sigma_1 - \sigma_2)$	h_γ	ϕ_γ^L	θ_p	ϕ_p	$\theta_{p'}$	$\phi_{p'}$
$d\sigma_0$		*unp*	*unp*	*unp*	*unp*	*unp*	*unp*
$2\hat{\Sigma}$	$\sigma_1 = \sigma(\perp, 0, 0)$	-	$\pi/2$	*unp*	*unp*	*unp*	*unp*
	$\sigma_2 = \sigma(\parallel, 0, 0)$	-	0	*unp*	*unp*	*unp*	*unp*
$2\hat{T}$	$\sigma_1 = \sigma(0, +y, 0)$	*unp*	*unp*	$\pi/2$	$\pi/2$	*unp*	*unp*
	$\sigma_2 = \sigma(0, -y, 0)$	*unp*	*unp*	$\pi/2$	$3\pi/2$	*unp*	*unp*
$\hat{P}$	$\sigma_1 = \sigma(0, 0, +y')$	*unp*	*unp*	*unp*	*unp*	$\pi/2$	$\pi/2$
	$\sigma_2 = \sigma(0, 0, -y')$	*unp*	*unp*	*unp*	*unp*	$\pi/2$	$3\pi/2$

TABLE VII: Observables with both beam and target polarization in their leading terms of Eq. (37); $d\sigma_0 = (1/2)(\sigma_1 + \sigma_2)$ and $\hat{A} = (1/2)(\sigma_1 - \sigma_2)$.

B-T		Beam		Target		Recoil	
Observable	$(\sigma_1 - \sigma_2)$	h_γ	ϕ_γ^L	θ_p	ϕ_p	$\theta_{p'}$	$\phi_{p'}$
$2\hat{E}$	$\sigma_1 = \sigma(+1, -z, 0)$	$+1$	-	π	0	*unp*	*unp*
	$\sigma_2 = \sigma(+1, +z, 0)$	$+1$	-	0	0	*unp*	*unp*
$2\hat{E}$	$\sigma_1 = \sigma(+1, -z, 0)$	$+1$	-	π	0	*unp*	*unp*
	$\sigma_2 = \sigma(-1, -z, 0)$	-1	-	π	0	*unp*	*unp*
$2\hat{G}$	$\sigma_1 = \sigma(+\pi/4, +z, 0)$	-	$\pi/4$	0	0	*unp*	*unp*
	$\sigma_2 = \sigma(+\pi/4, -z, 0)$	-	$\pi/4$	π	0	*unp*	*unp*
$2\hat{G}$	$\sigma_1 = \sigma(+\pi/4, +z, 0)$	-	$\pi/4$	0	0	*unp*	*unp*
	$\sigma_2 = \sigma(-\pi/4, +z, 0)$	-	$3\pi/4$	0	0	*unp*	*unp*
$2\hat{F}$	$\sigma_1 = \sigma(+1, +x, 0)$	$+1$	-	$\pi/2$	0	*unp*	*unp*
	$\sigma_2 = \sigma(-1, +x, 0)$	-1	-	$\pi/2$	0	*unp*	*unp*
$2\hat{F}$	$\sigma_1 = \sigma(+1, +x, 0)$	$+1$	-	$\pi/2$	0	*unp*	*unp*
	$\sigma_2 = \sigma(+1, -x, 0)$	$+1$	-	$\pi/2$	π	*unp*	*unp*
$2\hat{H}$	$\sigma_1 = \sigma(+\pi/4, +x, 0)$	-	$\pi/4$	$\pi/2$	0	*unp*	*unp*
	$\sigma_2 = \sigma(-\pi/4, +x, 0)$	-	$3\pi/4$	$\pi/2$	0	*unp*	*unp*
$2\hat{H}$	$\sigma_1 = \sigma(+\pi/4, +x, 0)$	-	$\pi/4$	$\pi/2$	0	*unp*	*unp*
	$\sigma_2 = \sigma(+\pi/4, -x, 0)$	-	$\pi/4$	$\pi/2$	π	*unp*	*unp*

TABLE VIII: Observables with both beam and recoil polarization in their leading terms in Eq. (37); $d\sigma_0 = (\sigma_1 + \sigma_2)$ and $\hat{A} = (\sigma_1 - \sigma_2)$.

B-R		Beam		Target		Recoil	
Observable	$(\sigma_1 - \sigma_2)$	h_γ	ϕ_γ^L	θ_p	ϕ_p	$\theta_{p'}$	$\phi_{p'}$
$\hat{C}_{x'}$	$\sigma_1 = \sigma(+1, 0, +x')$	$+1$	-	*unp*	*unp*	$\pi/2 + \theta_K$	0
	$\sigma_2 = \sigma(-1, 0, +x')$	-1	-	*unp*	*unp*	$\pi/2 + \theta_K$	0
$\hat{C}_{x'}$	$\sigma_1 = \sigma(+1, 0, +x')$	$+1$	-	*unp*	*unp*	$\pi/2 + \theta_K$	0
	$\sigma_2 = \sigma(+1, 0, -x')$	$+1$	-	*unp*	*unp*	$3\pi/2 + \theta_K$	0
$\hat{C}_{z'}$	$\sigma_1 = \sigma(+1, 0, +z')$	$+1$	-	*unp*	*unp*	θ_K	0
	$\sigma_2 = \sigma(-1, 0, +z')$	-1	-	*unp*	*unp*	θ_K	0
$\hat{C}_{z'}$	$\sigma_1 = \sigma(+1, 0, +z')$	$+1$	-	*unp*	*unp*	θ_K	0
	$\sigma_2 = \sigma(+1, 0, -z')$	$+1$	-	*unp*	*unp*	$\pi + \theta_K$	0
$\hat{O}_{x'}$	$\sigma_1 = \sigma(+\pi/4, 0, +x')$	-	$\pi/4$	*unp*	*unp*	$\pi/2 + \theta_K$	0
	$\sigma_2 = \sigma(-\pi/4, 0, +x')$	-	$3\pi/4$	*unp*	*unp*	$\pi/2 + \theta_K$	0
$\hat{O}_{x'}$	$\sigma_1 = \sigma(+\pi/4, 0, +x')$	-	$\pi/4$	*unp*	*unp*	$\pi/2 + \theta_K$	0
	$\sigma_2 = \sigma(+\pi/4, 0, -x')$	-	$\pi/4$	*unp*	*unp*	$3\pi/2 + \theta_K$	0
$\hat{O}_{z'}$	$\sigma_1 = \sigma(+\pi/4, 0, +z')$	-	$\pi/4$	*unp*	*unp*	θ_K	0
	$\sigma_2 = \sigma(-\pi/4, 0, +z')$	-	$3\pi/4$	*unp*	*unp*	θ_K	0
$\hat{O}_{z'}$	$\sigma_1 = \sigma(+\pi/4, 0, +z')$	-	$\pi/4$	*unp*	*unp*	θ_K	0
	$\sigma_2 = \sigma(+\pi/4, 0, -z')$	-	$\pi/4$	*unp*	*unp*	$\pi + \theta_K$	0

TABLE IX: Observables with both target and recoil polarization in their leading terms of Eq. (37); $d\sigma_0 = (\sigma_1 + \sigma_2)$ and $\hat{A} = (\sigma_1 - \sigma_2)$.

T-*R*		Beam		Target		Recoil	
Observable	$(\sigma_1 - \sigma_2)$	h_γ	ϕ_γ^L	θ_p	ϕ_p	$\theta_{p'}$	$\phi_{p'}$
$\hat{L}_{x'}$	$\sigma_1 = \sigma(0, +z, +x')$	*unp*	*unp*	0	0	$\pi/2 + \theta_K$	0
	$\sigma_2 = \sigma(0, -z, +x')$	*unp*	*unp*	π	0	$\pi/2 + \theta_K$	0
$\hat{L}_{x'}$	$\sigma_1 = \sigma(0, +z, +x')$	*unp*	*unp*	0	0	$\pi/2 + \theta_K$	0
	$\sigma_2 = \sigma(0, +z, -x')$	*unp*	*unp*	0	0	$3\pi/2 + \theta_K$	0
$\hat{L}_{z'}$	$\sigma_1 = \sigma(0, +z, +z')$	*unp*	*unp*	0	0	θ_K	0
	$\sigma_2 = \sigma(0, -z, +z')$	*unp*	*unp*	π	0	θ_K	0
$\hat{L}_{z'}$	$\sigma_1 = \sigma(0, +z, +z')$	*unp*	*unp*	0	0	θ_K	0
	$\sigma_2 = \sigma(0, +z, -z')$	*unp*	*unp*	0	0	$\pi + \theta_K$	0
$\hat{T}_{x'}$	$\sigma_1 = \sigma(0, +x, +x')$	*unp*	*unp*	$\pi/2$	0	$\pi/2 + \theta_K$	0
	$\sigma_2 = \sigma(0, -x, +x')$	*unp*	*unp*	$\pi/2$	π	$\pi/2 + \theta_K$	0
$\hat{T}_{x'}$	$\sigma_1 = \sigma(0, +x, +x')$	*unp*	*unp*	$\pi/2$	0	$\pi/2 + \theta_K$	0
	$\sigma_2 = \sigma(0, +x, -x')$	*unp*	*unp*	$\pi/2$	0	$3\pi/2 + \theta_K$	0
$\hat{T}_{z'}$	$\sigma_1 = \sigma(0, +x, +z')$	*unp*	*unp*	$\pi/2$	0	θ_K	0
	$\sigma_2 = \sigma(0, -x, +z')$	*unp*	*unp*	$\pi/2$	π	θ_K	0
$\hat{T}_{z'}$	$\sigma_1 = \sigma(0, +x, +z')$	*unp*	*unp*	$\pi/2$	0	θ_K	0
	$\sigma_2 = \sigma(0, +x, -z')$	*unp*	*unp*	$\pi/2$	0	$\pi + \theta_K$	0

Appendix C: The Fierz Identities

We list here the Fierz identities relating *asymmetries*, with corrected signs. The equation numbering sequence in Appendices C 1-C 3 is that of Chiang and Tabakin [1]. Compared to the latter, signs have changed in all but (L.1), (L.4-6), (Q.r), (Q.bt.3), (Q.tr.1-2), and of course the six *Squared* relations. Sign changes in eight of the equations can be attributed to the different definition for the E asymmetry used by Fasano, Tabakin and Saghai [11], to which Chiang and Tabakin refer. [We note that sign changes in another 15 equations could have been explained if the definition of the beam asymmetry (Σ) were also reversed; but our definition of Σ in Table A1 is identical to that of Fasano, Tabakin and Saghai [11].]

1. Linear-Quadratic relations

$$\begin{aligned} 1 =& \{\Sigma^2 + T^2 + P^2 + E^2 + G^2 + F^2 + H^2 \\ &+ O_{x'}^2 + O_{z'}^2 + C_{x'}^2 + C_{z'}^2 + L_{x'}^2 + L_{z'}^2 + T_{x'}^2 + T_{z'}^2\}/3. \end{aligned} \tag{L.0}$$

$$\Sigma = +TP + T_{x'}L_{z'} - T_{z'}L_{x'}. \tag{L.TR}$$

$$T = +\Sigma P - C_{x'}O_{z'} + C_{z'}O_{x'}. \tag{L.BR}$$

$$P = +\Sigma T + GF + EH. \tag{L.BT}$$

$$G = +PF + O_{x'}L_{x'} + O_{z'}L_{z'}. \tag{L.1}$$

$$H = +PE + O_{x'}T_{x'} + O_{z'}T_{z'}. \tag{L.2}$$

$$E = +PH - C_{x'}L_{x'} - C_{z'}L_{z'}. \tag{L.3}$$

$$F = +PG + C_{x'}T_{x'} + C_{z'}T_{z'}. \tag{L.4}$$

$$O_{x'} = +TC_{z'} + GL_{x'} + HT_{x'}. \tag{L.5}$$

$$O_{z'} = -TC_{x'} + GL_{z'} + HT_{z'}. \tag{L.6}$$

$$C_{x'} = -TO_{z'} - EL_{x'} + FT_{x'}. \tag{L.7}$$

$$C_{z'} = +TO_{x'} - EL_{z'} + FT_{z'}. \tag{L.8}$$

$$T_{x'} = +\Sigma L_{z'} + HO_{x'} + FC_{x'}. \tag{L.9}$$

$$T_{z'} = -\Sigma L_{x'} + HO_{z'} + FC_{z'}. \tag{L.10}$$

$$L_{x'} = -\Sigma T_{z'} + GO_{x'} - EC_{x'}. \tag{L.11}$$

$$L_{z'} = +\Sigma T_{x'} + GO_{z'} - EC_{z'}. \tag{L.12}$$

2. Quadratic relations

$$C_{x'}O_{x'} + C_{z'}O_{z'} + EG - FH = 0. \tag{Q.b}$$

$$GH - EF - L_{x'}T_{x'} - L_{z'}T_{z'} = 0. \tag{Q.t}$$

$$C_{x'}C_{z'} + O_{x'}O_{z'} - L_{x'}L_{z'} - T_{x'}T_{z'} = 0. \tag{Q.r}$$

$$\Sigma G - TF - O_{z'}T_{x'} + O_{x'}T_{z'} = 0. \tag{Q.bt.1}$$

$$\Sigma H - TE + O_{z'}L_{x'} - O_{x'}L_{z'} = 0. \tag{Q.bt.2}$$

$$\Sigma E - TH + C_{z'}T_{x'} - C_{x'}T_{z'} = 0. \tag{Q.bt.3}$$

$$\Sigma F - TG + C_{z'}L_{x'} - C_{x'}L_{z'} = 0. \tag{Q.bt.4}$$

$$\Sigma O_{x'} - PC_{z'} + GT_{z'} - HL_{z'} = 0. \tag{Q.br.1}$$

$$\Sigma O_{z'} + PC_{x'} - GT_{x'} + HL_{x'} = 0. \tag{Q.br.2}$$

$$\Sigma C_{x'} + PO_{z'} - ET_{z'} - FL_{z'} = 0. \tag{Q.br.3}$$

$$\Sigma C_{z'} - PO_{x'} + ET_{x'} + FL_{x'} = 0. \tag{Q.br.4}$$

$$TT_{x'} - PL_{z'} - HC_{z'} + FO_{z'} = 0. \tag{Q.tr.1}$$

$$TT_{z'} + PL_{x'} + HC_{x'} - FO_{x'} = 0. \tag{Q.tr.2}$$

$$TL_{x'} + PT_{z'} - GC_{z'} - EO_{z'} = 0. \tag{Q.tr.3}$$

$$TL_{z'} - PT_{x'} + GC_{x'} + EO_{x'} = 0. \tag{Q.tr.4}$$

3. Squared relations

$$G^2 + H^2 + E^2 + F^2 + \Sigma^2 + T^2 - P^2 = 1. \tag{S.bt}$$

$$O_{x'}^2 + O_{z'}^2 + C_{x'}^2 + C_{z'}^2 + \Sigma^2 - T^2 + P^2 = 1. \tag{S.br}$$

$$T_{x'}^2 + T_{z'}^2 + L_{x'}^2 + L_{z'}^2 - \Sigma^2 + T^2 + P^2 = 1. \tag{S.tr}$$

$$G^2 + H^2 - E^2 - F^2 - O_{x'}^2 - O_{z'}^2 + C_{x'}^2 + C_{z'}^2 = 0. \tag{S.b}$$

$$G^2 - H^2 + E^2 - F^2 + T_{x'}^2 + T_{z'}^2 - L_{x'}^2 - L_{z'}^2 = 0. \tag{S.t}$$

$$O_{x'}^2 - O_{z'}^2 + C_{x'}^2 - C_{z'}^2 - T_{x'}^2 + T_{z'}^2 - L_{x'}^2 + L_{z'}^2 = 0. \tag{S.r}$$

4. ARS-Squared relations

Here we include a set of squared relations from Artru, Richard and Soffer (ARS) [30]. These can be derived from combinations of relations in the preceding sections. For example, the first, (ARS.S.bt), can be obtained by combining Eqs. (S.bt) and (L.BT). Our relations differ in sign from ARS in those terms involving F, $C_{x'}$ and $C_{z'}$, and as a result there are sign differences in Eqs. (ARS.S.bt), (ARS.S.br) and (ARS.btr1).

$$(1 \pm P)^2 = (T \pm \Sigma)^2 + (E \pm H)^2 + (G \pm F)^2. \tag{ARS.S.bt}$$

$$(1 \pm T)^2 = (P \pm \Sigma)^2 + (C_{x'} \mp O_{z'})^2 + (C_{z'} \pm O_{x'})^2. \tag{ARS.S.br}$$

$$(1 \pm \Sigma)^2 = (P \pm T)^2 + (L_{x'} \mp T_{z'})^2 + (L_{z'} \pm T_{x'})^2. \tag{ARS.S.tr}$$

$$(1 \pm L_{z'})^2 = (\Sigma \pm T_{x'})^2 + (E \mp C_{z'})^2 + (G \pm O_{z'})^2. \tag{ARS.btr1}$$

$$(1 \pm T_{x'})^2 = (\Sigma \pm L_{z'})^2 + (F \pm C_{x'})^2 + (H \pm O_{x'})^2. \tag{ARS.btr2}$$

Appendix D: Born amplitudes for $\gamma N \to K\Lambda$

In this Appendix, we summarize the Born amplitudes for $\gamma(q) + p(p) \to K^+(k') + \Lambda(p')$ in the center of mass energy ($\vec{p} = -\vec{q}$, $\vec{p}' = -\vec{k}'$), which are used to fix high partial waves ($4 \le L \le 8$) in the multipole analyses presented in Sec. VIII. We consider the following Born terms for $I^\mu \epsilon_\mu$ [see the paragraph including Eq. (6) for the description of $I^\mu \epsilon_\mu$]:

$$I^\mu \epsilon_\mu = I_a + I_b + I_c + I_d + I_e + I_f, \tag{D1}$$

where

$$I_a = i\frac{f_{KN\Lambda}}{m_K}\ \not{k}'\gamma_5\frac{1}{\not{p}'+\not{k}'-m_N}\Gamma_N(q^2)F(|\vec{k}'|,\Lambda_{KN\Lambda}), \tag{D2}$$

$$I_b = i\frac{f_{KN\Lambda}}{m_K}\Gamma_\Lambda(q^2)\frac{1}{\not{p}-\not{k}'-m_\Lambda}\ \not{k}'\gamma_5 F(|\vec{k}'|,\Lambda_{KN\Lambda}), \tag{D3}$$

$$I_c = i\frac{f_{KN\Sigma}}{m_K}\Gamma_{\Lambda\Sigma}(q^2)\frac{1}{\not{p}-\not{k}'-m_\Sigma}\ \not{k}'\gamma_5 F(|\vec{k}'|,\Lambda_{KN\Sigma}), \tag{D4}$$

$$I_d = -ie\frac{f_{KN\Lambda}}{m_K}\ \not{\epsilon}_\gamma\gamma_5 F(|\vec{k}'|,\Lambda_{KN\Lambda}), \tag{D5}$$

$$I_e = ie\frac{f_{KN\Lambda}}{m_K}\frac{\tilde{\not{k}}\gamma_5}{\tilde{k}^2-m_K^2}(\tilde{k}+k')\cdot\epsilon_\gamma F(|\vec{\tilde{k}}|,\Lambda_{KN\Lambda}), \tag{D6}$$

$$\begin{aligned} I_f &= -e\frac{g_{K^*N\Lambda}g_{K^*K^+\gamma}}{m_K}[\gamma^\delta+\frac{\kappa_{K^*N\Lambda}}{2(m_N+m_\Lambda)}(\gamma^\delta\ \tilde{\not{k}}-\tilde{\not{k}}\gamma^\delta)] \\ &\quad\times\epsilon_{\alpha\beta\eta\delta}\tilde{k}^\eta q^\alpha\epsilon_\gamma^\beta\frac{1}{\tilde{k}^2-m_{K^*}^2}F(|\vec{\tilde{k}}|,\Lambda_{K^*N\Lambda}), \end{aligned} \tag{D7}$$

with $\tilde{k}=p-p'$ and

$$\Gamma_N = e\{\not{\epsilon}_\gamma-\frac{\kappa_N}{4m_N}[\not{\epsilon}_\gamma\ \not{q}-\not{q}\ \not{\epsilon}_\gamma]\}, \tag{D8}$$

$$\Gamma_\Lambda = -e\frac{\kappa_\Lambda}{4m_N}[\not{\epsilon}_\gamma\ \not{q}-\not{q}\ \not{\epsilon}_\gamma], \tag{D9}$$

$$\Gamma_{\Lambda\Sigma} = -e\frac{\kappa_{\Lambda\Sigma}}{4m_N}[\not{\epsilon}_\gamma\ \not{q}-\not{q}\ \not{\epsilon}_\gamma]. \tag{D10}$$

Also, we have introduced the dipole form factors $F(|\vec{k}|,\Lambda)$ for the hadronic vertex defined as

$$F(|\vec{k}|,\Lambda) = \left(\frac{\Lambda^2}{|\vec{k}|^2+\Lambda^2}\right)^2. \tag{D11}$$

We make use of the SU(3) relation for the coupling constants,

$$\frac{f_{KN\Lambda}}{m_K} = \frac{f_{\pi NN}}{m_\pi}\frac{-3+2\alpha}{\sqrt{3}}, \tag{D12}$$

$$\frac{f_{KN\Sigma}}{m_K} = \frac{f_{\pi NN}}{m_\pi}\frac{3-4\alpha}{\sqrt{3}}, \tag{D13}$$

$$g_{K^*N\Lambda} = g_{\rho NN}\frac{-3+2\alpha}{\sqrt{3}}, \tag{D14}$$

$$\frac{\kappa_{K^*N\Lambda}}{m_N+m_\Lambda} = \frac{\kappa_\rho}{2m_N}, \tag{D15}$$

and take parameters as $f_{\pi NN}=\sqrt{0.08\times 4\pi}$, $\kappa_p=\mu_p-1=1.79$, $\alpha=0.635$, $g_{\rho NN}=8.72$, $\kappa_\rho=2.65$, $g_{\gamma K^*K^+}/m_K=0.254\mathrm{GeV}^{-1}$, $\kappa_\Lambda=-0.61$, and $\kappa_{\Lambda\Sigma}=-1.61$. As for the cutoff factors, we take $\Lambda_{KN\Lambda} = \Lambda_{KN\Sigma} = \Lambda_{K^*N\Lambda} = 500$ MeV.

---

[1] W.-T. Chiang and F. Tabakin, Phys. Rev. C **55**, 2054 (1997).

[2] *The g9-FROST series of experiments*, URL `http://clasweb.jlab.org/shift/g9/` .

[3] *The g14-HDice experiment*, URL `http://www.jlab.org/exp_prog/proposals/06/PR-06-101.pdf` .

[4] A. Lleres *et al.*, Eur. Phys. J. A **31**, 79 (2007).

[5] A. Lleres *et al.* (GRAAL Collaboration), Eur. Phys. J. A **39**, 149 (2009).

[6] G. F. Chew, M. L. Goldberger, F. E. Low, and Y. Nambu, Phys. Rev. **105**, 1345 (1957).

[7] I. S. Barker, A. Donnachie, and J. K. Storrow, Nucl. Phys. **B95**, 347 (1975).

[8] A. Donnachie and G. Shaw, Appl. Phys. **37**, 333 (1966).

[9] A. Donnachie, in *Pure and Applied Physics*, edited by E. H. S. Bishop (Academic Press, New York, 1972), Vol. 25-V, p. 1.

[10] R. A. Adelseck and B. Saghai, Phys. Rev. C **42**, 108 (1990).

[11] C. G. Fasano, F. Tabakin, and B. Saghai, Phys. Rev. C **46**, 2430 (1992).

[12] D. Drechsel and L. Tiator, J. Phys. G **18**, 449 (1992).

[13] G. Knochlein, D. Drechsel, and L. Tiator, Z. Phys. A **352**, 327 (1995).

[14] J. D. Jackson, *Classical Electrodynamics* (John Wiley & Sons, New York, 1975).

[15] J. D. Bjorken and S. D. Drell, *Relativistic Quantum Mechanics* (McGraw-Hill, New York, 1964).

[16] M. Jacob and G. C. Wick, Ann. Phys. **7**, 404 (1959); **281**, 774 (2000).

[17] D. M. Brink and G. R. Satchler, *Angular Momentum* (Oxford University Press, Oxford, 1968).

[18] S. Hoblit *et al.* (LEGS-Spin Collaboration), Phys. Rev. Lett. **102**, 172002 (2009), and references therein.

[19] R. K. Bradford *et al.* (CLAS Collaboration), Phys. Rev. C **75**, 035205 (2007).

[20] T. D. Lee and C. N. Yang, Phys. Rev. **108**, 1645 (1957).

[21] K. Nakamura *et al.* (Particle Data Group), J. Phys. G **37**, 075021 (2010).

[22] *MAID and Kaon-MAID isobar models of meson production*, URL `http://wwwkph.kph.uni-mainz.de/MAID/`.

[23] D. Drechsel, S. S. Kamalov, and L. Tiator, Eur. Phys. J. A **34**, 69 (2007).

[24] T. Mart and C. Bennhold, Phys. Rev. C **61**, 012201 (1999).

[25] *SAID partial wave analysis facility*, URL `http://gwdac.phys.gwu.edu/`.

[26] R. A. Arndt, W. J. Briscoe, I. I. Strakovsky, and R. L. Workman, Phys. Rev. C **66**, 055213 (2002).

[27] A. V. Anisovich, E. Klempt, V. A. Nikonov, M. A. Matveev, A. V. Sarantsev, and U. Thoma, Eur. Phys. J. A **44**, 203 (2010); arXiv:0911.5277v2; *Bonn-Gatchina Partial Wave Analysis*, URL `http://pwa.hiskp.uni-bonn.de/` .

[28] B. Juliá-Díaz, B. Saghai, T.-S. H. Lee, and F. Tabakin, Phys. Rev. C **73**, 055204 (2006).

[29] X. Artru, J.-M. Richard, and J. Soffer, Phys. Rev. C **75**, 024002 (2007).

[30] X. Artru, M. Elchikh, J.-M. Richard, J. Soffer, and O. V. Teryaev, Phys. Rep. **470**, 1 (2009).

[31] D. Ireland (private communication).

[32] K. K. Glander *et al.* (SAPHIR Collaboration), Eur. Phys. J. A **19**, 2 (2004).

[33] M. E. McCracken *et al.* (CLAS Collaboration), Phys. Rev. C **81**, 025201 (2010).

[34] R. K. Bradford *et al.* (CLAS Collaboration), Phys. Rev. C **73**, 035202 (2006).

[35] R. G. T. Zegers *et al.* (LEPS Collaboration), Phys. Rev. Lett. **91**, 92001 (2003).

[36] G. Blanpied *et al.* (LEGS Collaboration), Phys. Rev. C **64**, 25203 (2001).

[37] J. E. Bowcock and H. Burkhardt, Rep. Prog. Phys. **38**, 1099 (1975).

[38] A. V. Anisovich, V. Kleber, E. Klempt, V. A. Nikonov, A. V. Sarantsev, and U. Thoma, Eur. Phys. J. A **34**, 243 (2007).

[39] H. Kamano, hkamano@jlab.org .